The influence of fluid-structure interaction on cloud cavitation about a stiff hydrofoil (part 1)

Samuel M. Smith[1]†, James A. Venning[1], Bryce W. Pearce[1], Yin Lu Young[2] and Paul A. Brandner[1]

[1]Australian Maritime College, University of Tasmania, Launceston, Tasmania, Australia

[2]Department of Naval Architecture and Marine Engineering, University of Michigan, Ann Arbour, MI, USA

(Received 17/9/2019; revised 20/11/2019; accepted 9/12/2019)

The physics associated with various cavitation regimes about a hydrofoil are investigated in a variable-pressure water tunnel using high-speed photography and synchronized force measurements. Experiments were conducted on a relatively stiff stainless steel hydrofoil at $Re = 0.8 \times 10^6$ for cavitation numbers, σ, ranging from 0.2 to 1.2, with the hydrofoil experiencing sheet, cloud and super-cavitation regimes. The NACA0009 model of tapered planform was vertically mounted in a cantilevered configuration to a six-component force balance at an incidence, α, of 6° to the oncoming flow. Tip deformations and cavitation behaviour were recorded with synchronized force measurements utilizing two high-speed cameras mounted underneath and to the side of the test section. Break-up and shedding of an attached cavity was found to be due to either interfacial instabilities, re-entrant jet formation, shockwave propagation or a complex coupled mechanism, depending on σ. Three primary shedding modes are identified. The Type IIa & IIb re-entrant jet driven oscillations exhibiting a linear dependence on σ, decreasing in frequency with decreasing σ due to growth in the cavity length, occurring at higher σ values (Type IIa: 0.4-1.0; Type IIb: 0.7-0.9). Shockwave-driven Type I shedding occurs for lower σ values (0.3-0.6) with the oscillation frequency being practically independent of σ. The Type IIa oscillations locked in to the first sub-harmonic of the hydrofoil's first bending mode in water which has been modulated due to the reduced added mass of the vapour cavity. Supplementary movies are available with the online version of the paper.

1. Introduction

The increasing importance of flow-induced vibrations over time is being driven by advancements in materials technology and ever increasing optimisation, resulting in structures becoming lighter, more flexible and susceptible to vibrations (Blevins 1977). Flow induced vibration phenomena have a profound influence on the the performance of the vast range of aerodynamic and hydrodynamic objects and are therefore significant in geometrical and structural design (Bisplinghoff *et al.* 1955). Cavitation about a hydrofoil involves a range of complex dynamical phenomena including mass transfer via phase change and diffusion, shockwaves, large and small-scale instabilities and turbulence, some of which are discernible in figure 1. These phenomena have the potential to cause significant and destructive vibrations (Franc & Michel 2004). Understanding these fluid-structure interaction (FSI) phenomena is of interest as flow over a lifting body can significantly alter the performance of maritime propulsion and control systems.

† Email address for correspondence: ssmith18@utas.edu.au

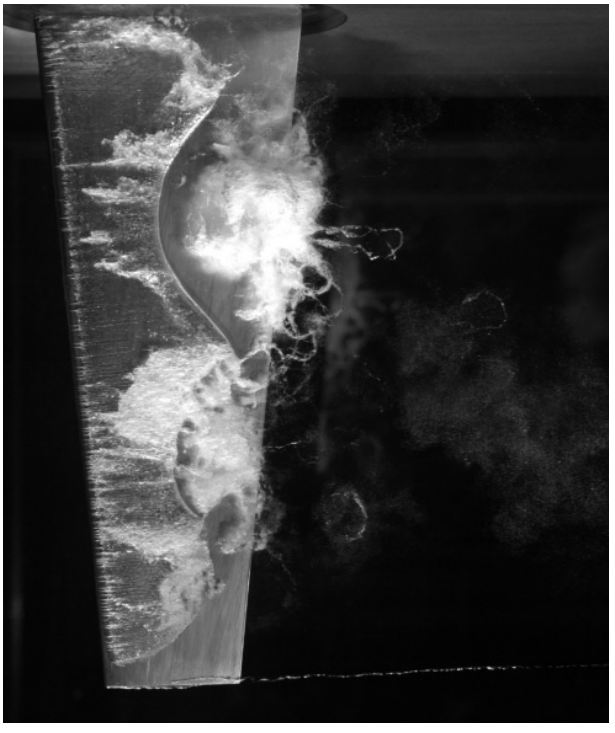

FIGURE 1. Cloud cavitation about a finite-span stainless steel hydrofoil exhibiting multiple shedding events along the span due to the re-entrant jet instability and spanwise compatibility of the cavitation. The hydrofoil is vertically mounted at an incidence of 6° to the flow with $Re = 0.8 \times 10^6$ and $\sigma = 0.7$.

Experimental studies investigating the influence of cavitation on flexible (i.e. compliant) hydrofoil's has previously been conducted by Kaplan & Lehman (1966); Brennen *et al.* (1980); Ausoni *et al.* (2007); Ducoin *et al.* (2012) with Kaplan & Lehman (1966) first observing modest vibration amplitudes due to cavitation about a hydrofoil. Examining the coupling between the hydro-elasticity and the trailing-edge vortex cavitation, Ausoni *et al.* (2005, 2007) observed that not only does the cavitation influence the structural vibrations, but the structural vibrations also affect cavitation behaviour. Numerical simulations by Akcabay & Young (2014) modelling the bending and torsional compliance of a cantilevered hydrofoil revealed maximum force and deflection fluctuations occurred when the maximum cavity length approaches the trailing-edge. Additionally, hydrofoil compliance was seen to increase the cavity length, thus decreasing the cavitation shedding frequency. However, the influence of compliance was only significant when the cavity length was near the trailing-edge. The unsteady two-phase flow has effect on the spectral content of a compliant hydrofoil compared to a relatively stiff one, causing frequency modulation (Akcabay & Young 2015), broadening of the frequency content (Akcabay *et al.* 2014) and leading to phenomena such as lock-in that leads to significant amplification of vibrations (Kato *et al.* 2006; Akcabay & Young 2015).

Cloud cavitation was first extensively investigated by Knapp (1955) where the detachment of a vapour cloud from an attached cavity due to a re-entrant jet was observed. Since then, several mechanisms have been identified as potential instabilities causing periodic shedding, depending on the flow conditions, in a particular streamwise pressure gradient. These included growth of interfacial instabilities such as Kelvin-Helmholtz waves (Bren-

nen 1969; Avellan *et al.* 1988; Brandner *et al.* 2010), re-entrant jet formation (Furness & Hutton 1975; Le *et al.* 1993; Kawanami *et al.* 1997; Stutz & Reboud 1997; Pham *et al.* 1999; Callenaere *et al.* 2001; Laberteaux & Ceccio 2001*a*,*b*; Smith *et al.* 2017, 2018, 2019), and shock propagation (Jakobsen 1964; Reisman *et al.* 1998; Ceccio 2015; Ganesh *et al.* 2016; Smith *et al.* 2018). In certain conditions, multiple instabilities can be present simultaneously with Ganesh *et al.* (2016) showing both bubbly shock propagation and re-entrant jet flow from measurements of the void fraction field with X-ray densiotmetry. In addition, Brandner *et al.* (2010), and more recently de Graaf *et al.* (2017), using high-speed photography observed all three mechanisms either occurring in isolation or as a complex, coupled mechanism in cloud cavitation about a sphere. Furthermore, experiments on a NACA0015 hydrofoil revealed complex multi-stage shedding cycles involving both re-entrant jet and shockwave instabilities (Venning *et al.* 2017, 2018*b*).

A re-entrant jet forms by flow over the cavity interface forming an instantaneous stagnation on the wall associated with the cavity closure, resulting in some flow directed back upstream along the hydrofoil surface (Brennen 1995). The re-entrant jet travels upstream towards the cavity detachment until it impinges upon and breaks up the cavity surface, resulting in a detached cavity that is advected downstream as a bubbly mixture, termed a 'cloud' structure due to its similarity in visual appearance. As mentioned previously, the re-entrant jet shedding mechanism has been extensively studied and it has been found that for re-entrant jet driven cloud cavitation to occur, the cavity needs to close in a region with a sufficiently large adverse pressure gradient as well as being thick enough to limit interaction between the re-entrant jet and the cavity interface (Franc 2001). Cloud cavitation driven by the re-entrant jet instability, referred to as Type II oscillation in literature, has a shedding frequency that is dependant on the cavity length, and therefore σ as well as incidence, α (Callenaere *et al.* 2001). In the case of a hydrofoil, the cavity closes in a reducing adverse pressure gradient as it grows and approaches the trailing-edge. This leads to degradation of the re-entrant jet and a transition of the primary instability driving shedding to a shockwave instability (Kjeldsen & Arndt 2001).

As the attached cavity grows on a hydrofoil, a change in the shedding mechanism is observed with the re-entrant jet instability transitioning to a shockwave instability. Shockwave driven cloud cavitation, referred to as Type I oscillations (Kjeldsen & Arndt 2001), occurs when a reduction in σ or increase in α causes increased cavity size and significant reduction in local void fraction to allow shockwave formation and propagation from the collapse of bubbles. For shockwave formation and propagation, the shed clouds need to be densely populated with bubbles that interact and collapse coherently (Reisman *et al.* 1998). Additionally, the sound speed of the liquid-vapour mixture is required to fall below the local flow speed (Ganesh *et al.* 2016; Wu *et al.* 2019). This can occur under cavitating conditions as the presence of bubbles increases the local void fraction which has been shown to significantly reduce the speed of sound in the bubbly mixture (Shamsborhan *et al.* 2010). These conditions are met when the cavity has increased in size to shed large-scale vapour structures that raise the local void fraction sufficiently.

To reduce the complexity of the cavitation dynamics in three-dimensional (3D) flows, a large number of past studies have focused on two-dimensional (2D) flows. However, even in the 2D case, the resulting shedding physics still exhibit significant 3D characteristics, as observed by Kubota *et al.* (1989); de Lange & de Bruin (1998); Kawanami *et al.* (1998), resulting in spanwise variations of the cloud cavitation. Furthermore, Kawanami *et al.* (1998) show that cloud cavitation can have a spanwise spatial periodicity on a 2D hydrofoil where periodic shedding occurs at multiple locations along the span, depending on the streamwise length of the cavity. This is also observed by Prothin *et al.* (2016) and Smith *et al.* (2018, 2019) showing multiple stable shedding locations along a finite-

span hydrofoil, highlighting the role of compatibility between the cavity length and the span first noted by Kawanami *et al.* (1998). In both 2D and 3D flows, incompatible cavity lengths are seen to result in incoherent shedding along the span (Kawanami *et al.* 1998; Kjeldsen *et al.* 2000; Smith *et al.* 2018; Harwood *et al.* 2019*a*). The formation of stable shedding sites is seen to be reinforced by the spanwise component of shedding mechanisms, such as re-entrant jets, as they prevent other instabilities from interfering in the local shedding process (de Lange & de Bruin 1998).

Investigations into the effect of hydrofoil planform geometry by Ihara *et al.* (1989) have shown sweep to minimise lift and drag force fluctuations associated with the absence of large cavity break-off that is observed on an unswept hydrofoil. Furthermore, the highly swept hydrofoil is seen to confine full-chord cloud cavitation to the downstream portion of the hydrofoil, with the upstream portion forming a stable cavity. This cavitation behaviour is due to the strong spanwise flow component redirecting the re-entrant jet away from the cavity detachment, thus preventing cavity break-off and allowing a stable cavity to form (Laberteaux & Ceccio 2001*b*). Time-resolved particle image velocimetry experiments on a 3D hydrofoil by Foeth *et al.* (2006) also shows significant cavitation stability sensitivity due to 3D flow effects. The influence on cloud cavitation of a free tip, tapered planform and spanwise cavity oscillations remain largely to be investigated, despite several investigations into the effect of a varying spanwise geometry.

This research consists of two parts and is devoted to understanding the influence of FSI on cloud cavitation about a hydrofoil. Cavitating conditions are achieved about the vertically mounted cantilevered hydrofoil through precise pressure control of the variable-pressure water tunnel. Forces acting on the hydrofoil were acquired simultaneously with tip deflections and cavitation behaviour measurements using high-speed photography at various cavitation regimes by varying the freestream water tunnel pressure. The results produce further insight and correlation between the shedding physics, hydrofoil loading and structural deformations. Part I is dedicated to establishing a reference through utilising a relatively stiff hydrofoil whereby the deformations are small compared to the dimensions. Hence, structural dynamics of the hydrofoil have minimal effect on the loading and cavity dynamics. Part II investigates the influence of FSI by utilising a compliant hydrofoil with observations informed by those made on the relatively stiff reference in Part I.

2. Experimental Overview

2.1. *Experimental Facility*

Measurements were undertaken at the Australian Maritime College in the Cavitation Research Laboratory variable-pressure water tunnel. The tunnel test section measures 0.6 m square by 2.6 m long in which the operating velocity and absolute pressure can be varied from 2 to 12 m/s and 4 to 400 kPa, respectively. The medium sized tunnel contains 365 m^3 of demineralized water. While there is a permanent background nuclei population present in the water, these are of sufficiently high strength and sparsity to be considered inactive in this flow (Venning *et al.* 2018*c*). The circuit architecture has been developed for continuous elimination of nuclei achieved through a combination of coalescence/gravity separation in a downstream tank and dissolution via extended residence in a resorber (Brandner 2018). This allows consistent long duration measurements as the oncoming recirculated flow is free from nuclei produced from the cavitating hydrofoil that might influence the cavitation behaviour, as observed by Arndt & Keller (2003); Russell *et al.* (2018). A detailed description of the facility is given in Brandner *et al.* (2007).

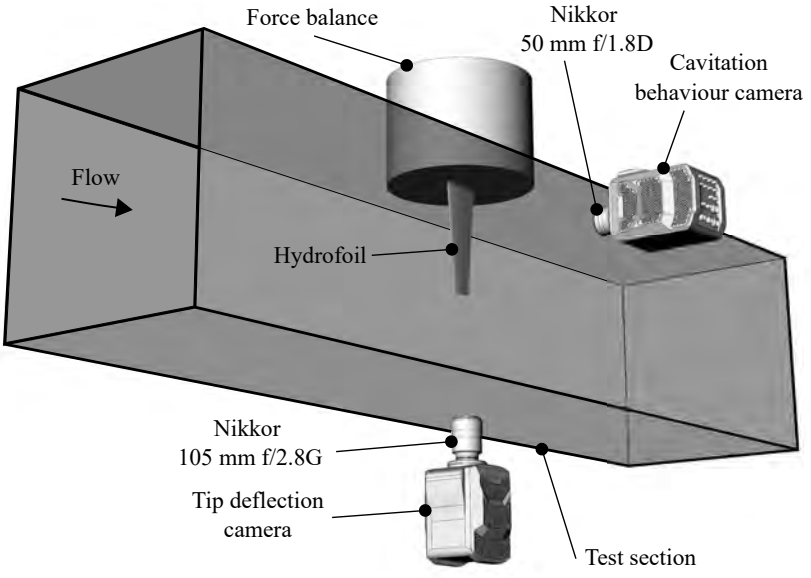

FIGURE 2. Experimental setup whereby the hydrofoil is attached to a force balance and mounted vertically on the test section ceiling. Cavitation behaviour and tip deflections were recorded using high-speed photography utilizing two Phantom v2640 high-speed cameras mounted on the side and below the test section, respectively.

Measurements were taken at a fixed incidence, α, of 6° and a chord-based Reynolds number, $Re = U_\infty \bar{c}/\nu$, equal to 0.8×10^6, where $\bar{c}$ is the mean chord, U_∞ is the freestream velocity and ν is the kinematic viscosity of the water. The cavitation number, $\sigma = 2(p_\infty - p_\mathrm{v})/\rho U_\infty^2$, where p_∞ is the absolute static pressure at the level of the hydrofoil tip, p_v is the vapour pressure, and ρ is the water density, was incrementally varied from 1.2 to 0.2 to investigate various cavitation regimes. Dissolved oxygen levels were kept between $3 - 4$ ppm for all measurements.

2.2. *Model Hydrofoil*

The model hydrofoil was mounted vertically on the centreline, 1.3 m downstream of the test section entrance through a 160 mm diameter penetration in the ceiling. A schematic of the experimental setup is shown in figure 2. The hydrofoil was attached to a six-component force balance, with an estimated precision of 0.1%, via a housing which clamped the hydrofoil into place using two profiled plates (figure 3). The penetration is made fair (to 50 μm) using an acrylic disk mounted to the measurement side of the force balance. The fairing disk has a 0.5 mm radial clearance to avoid interference with the force measurement. This type of mounting arrangement was implemented to accommodate the manufacturing of composite models used in part 2 and to ensure common fixed-end conditions for comparative measurements between the stainless steel and composite models (Zarruk *et al.* 2014).

The geometric and mechanical properties of the hydrofoil have been selected based on the requirements for modeling the static and dynamic FSI typical of control surfaces and propellers. The hydrofoil features a symmetric (unswept) trapezoidal planform of 300 mm span, b, with a 60 mm tip chord, c_tip, and 120 mm root chord, c_root, resulting in a mean chord, $\bar{c} = (c_\mathrm{root} + c_\mathrm{tip})/2$, of 90 mm. This gives an aspect ratio $(b/\bar{c})$ of 3.33, typical of marine propellers. The model has a modified NACA0009 section profile that features a

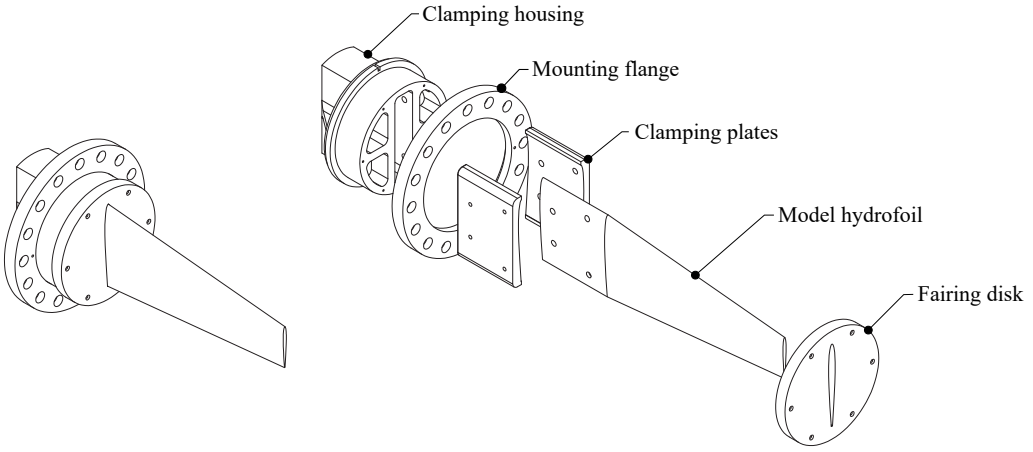

FIGURE 3. Hydrofoil model assembly showing an exploded view of the clamping housing arrangement that allows continuity of the model.

Fluid	Technique	Mount	f_n (Hz)	$St_n = f_n c/U_\infty$
Air	Impact / Accelerometer	Rigid	96	0.90
Water	DIC	Rigid	62	0.58
Water	DIC	Force balance	57	0.53
Water	Force measurements	Force balance	54	0.51

TABLE 1. First mode frequencies in bending of the NACA0009 stainless steel hydrofoil for various conditions as reported by Clarke *et al.* (2014). The in-water (fully wetted) measurements were made using Digital Image Correlation (DIC) and force measurements and the in-air using impact/accelerometer.

thicker trailing-edge for improved robustness against trailing-edge damage and to allow for manufacturing of the compliant composite models (Zarruk *et al.* 2014). Experiments performed by Zarruk *et al.* (2014) show that the modified profile has minimal effect on the forces and deflections experienced by the hydrofoil compared to the original NACA0009 profile. The stainless steel model was machined from a billet of Type 316 stainless steel and manufactured to a ± 0.1 mm surface tolerance and 0.8 µm surface finish.

The normal force, N, and pitching moment, P, acting on the hydrofoil are presented as dimensionless coefficients as $C_N = 2N/\rho U_\infty^2 \bar{c} b$ and $C_P = 2P/\rho U_\infty^2 \bar{c}^2 b$, respectively, with the coordinate system presented in figure 4(a). The hydrofoil first mode is in bending as shown by Clarke *et al.* (2014) and measured frequencies for various conditions and techniques are summarised in table 1. These results show the difference in frequencies for in-air, fully wetted and the influence of mounting compliance. The natural frequency, f_n, reduces by about 10% when mounted from the force balance compared with rigid mounting. Excitation of the first mode should then be expected to occur between $St_n = f_n \bar{c}/U_\infty$ values of about 0.5 and 0.9 depending on cavity extent affecting added mass as marked on figure 8.

2.3. *Experimental Techniques*

To obtain detailed information of loading variations on the hydrofoil through various cavitation regimes, long-duration force measurements were made at σ increments of 0.025. Tip deflection and cavitation behaviour measurements, discussed further below, were

Run Type	σ	T (s)	f_{HSP} (Hz)	f_{FB} (Hz)
Long	0.2-(0.025)-1.2	360	N/A	1 000
Medium	0.2-(0.1)-1.2, 0.65, 0.75	36	500	500
Short	0.2-(0.1)-1.2, 0.65, 0.75	1	6 600	6 600

TABLE 2. Test matrix for the various run types detailing the σ range, run duration, T, high-speed photography frame rate, f_{HSP}, and force balance sampling rate, f_{FB}. The Long acquisition periods provided high-resolution loading behaviour with σ. Due to camera storage limitations, simultaneous force measurement and high-resolution imaging of the cavitation behaviour and tip deflections was obtained with the Medium and Short run types, respectively.

obtained simultaneously (including force measurements) using high-speed photography at σ increments of 0.1. For these simultaneous measurements, due to limitations with respect to camera memory storage, 'medium' length, reduced temporal resolution runs were acquired suitable for statistical analysis of the imaging data sets and 'short' length, high temporal resolution data sets were acquired for a detailed analysis of the cavitation physics. Details of all three run types are summarised in table 2.

The force time-series were analysed using the continuous wavelet transform, following the procedure of Torrence & Compo (1998). The Morlet wavelet was applied and correlated at various scales with the time series, allowing events and intermittent components in the force and tip displacement history to be identified. Time-series data is presented with time, t, being non-dimensionalized as $t' = tU_\infty/\bar{c}$.

2.3.1. *Tip deflection*

The tip deflection of the hydrofoil was measured via high-speed photography utilizing a Phantom v2640 with a Nikkor 105 mm f/2.8G lens (figure 2). Operating with a resolution of 512 × 1 504 pixels and a spatial resolution of 0.049 mm/px. The tip deflection was determined using edge detection of the hydrofoil tip profile and comparing each frame to the hydrofoil under zero load based on the assumption that the profile locally remains undeformed. The edge detection process involved first rotating each frame by the angle of the hydrofoil under zero load relative to the frame using bicubic interpolation and then applying a 2-D Gaussain filter to smooth the image. The edge was detected along the profile based on peaks in the pixel intensity gradient along each row. Outliers were identified as being more than three standard deviations away from the local mean within a 50 element window and replaced using linear interpolation. The difference between the loaded and unloaded case gave the tip deflection with tip bending displacement, δ, taken as the average distance of every row with the twist, θ, determined from a line of best fit through the data with the tip displacement subtracted. Positive δ is defined as translation towards the suction side with positive θ defined as nose-up, as shown in figure 4. For the stainless steel model, no twist was clearly resolved within the precision of the method employed, indicating it is negligible, as was also reported by Zarruk *et al.* (2014) using high-resolution still photography for static deflections.

2.3.2. *Cavitation behaviour*

The cavitation behaviour over the suction side of the hydrofoil was recorded using a second Phantom v2640 high-speed camera with a Nikkor 50 mm f/1.8D lens (figure 2). The camera was operated with a resolution of 2048 × 1952 pixels and a spatial resolution of 0.185 mm/px with the same optical arrangement used for both the medium and short run acquisition types.

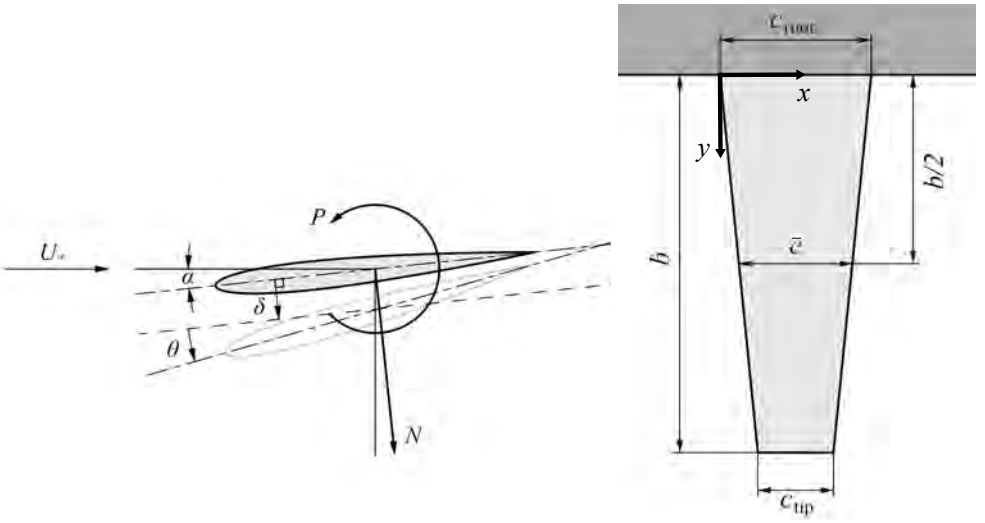

FIGURE 4. Coordinate system used for both the forces and tip deflection of the hydrofoil (left) is located at the mid-chord along the centreline. The deformed hydrofoil tip is represented by the dotted outline where the tip bending displacement, δ, is measured by taking the mean displacement of the profile edge perpendicular to the centreline at the zero-load case. The tip twist deflection, θ, is the rotation of the profile centreline from the zero-load case. A schematic of the hydrofoil's tapered planform (right) shows the coordinate system used in the analysis of the cavitation behaviour (e.g. cavity length) is located at the leading edge of the root chord.

To identify coherent structures in the dynamic cloud cavitation behaviour, spectral proper orthogonal decomposition (SPOD) is employed using the technique outlined by Towne *et al.* (2018). In this instance the SPOD is applied to the time varying image intensity as opposed to time varying velocity data from time resolved particle image velocimetry as typically used. SPOD optimally represents the space-time flow statistics by identifying energy ranked modes that are dynamically significant (Schmidt *et al.* 2018). Each high-speed photography acquisition provided time varying data (with image sequence) of the spatial variation (2 dimensional) of pixel intensity. Due to light scattering from interfacial surfaces, a high intensity was recorded where there was the presence of a cavity or bubbly mixture/shed cloud. Analyzing these image data sets with SPOD allowed for the identification of various shedding modes, both in frequency content and the spatial location.

SPOD utilizes multiple realizations of the temporal Fourier transform of the flow field, in this case the dynamic behaviour of the cavity, to obtain convergent estimates of the spectral densities by appropriately averaging the spectra, achieved using Welch's method (Welch 1967) with a Hanning window. The decomposition was performed on the high-speed photography data, consisting of n_x rows and n_y columns, obtained from the medium run types at each σ . The pixel intensity time series of each pixel was broken up into blocks with a length, N_f, of 256 snapshots, representing 0.512 s. The overlap between blocks, N_o, was 128 snapshots, representing 0.256 s. This results in 128 blocks, N_b, for the 18 000 snapshot long sequence, and producing a frequency resolution of 1.95 Hz for the extracted SPOD modes.

An overview of the SPOD calculation procedure applied to the data is given in the following with a detailed description of the SPOD methodology and algorithm given by Towne *et al.* (2018). For the n^{th} block, the matrix, $\boldsymbol{Q}^{(n)}$, is built from a portion of the high-speed movie, reshaped to have as many rows as pixels, $N = n_x \times n_y$, and N_f

columns, being the number of frames in each block. Each block is structured with the k^{th} frame in the n^{th} block represented as $\boldsymbol{q}_k^{(n)}$ (equation 2.1). These are considered to be statistically independent realizations of the flow under the ergodic hypothesis.

$$\boldsymbol{Q}^{(n)} = [\boldsymbol{q}_1^{(n)}, \boldsymbol{q}_2^{(n)}, ..., \boldsymbol{q}_{N_f}^{(n)}] \in \mathbb{R}^{N \times N_f} \tag{2.1}$$

Once the data matrix is correctly structured into N_b blocks, the Fourier transform is calculated for the n^{th} block using equation 2.2. Each block is then structured again as shown in equation 2.3 with $\hat{\boldsymbol{q}}_k^{(n)}$ being the n^{th} realization of the Fourier transform at the k^{th} discrete frequency.

$$\hat{\boldsymbol{q}}_k^{(n)} = \frac{1}{2N_f} \sum_{j=1}^{N_f} w_j \boldsymbol{q}_j^{(n)} e^{i2\pi(k-1)[(j-1)/N_f]} \tag{2.2}$$

$$\hat{\boldsymbol{Q}}^{(n)} = [\hat{\boldsymbol{q}}_1^{(n)}, \hat{\boldsymbol{q}}_2^{(n)}, ..., \hat{\boldsymbol{q}}_{N_f}^{(n)}] \tag{2.3}$$

The scalar weights, w_j, are nodal values of the Hanning window function that can be used to reduce spectral leakage due to non-periodicity of the data in each block.

For each frequency, k, the Fourier coefficients of each block are collected into the new matrix $\hat{\boldsymbol{Q}}_{f_k}$, as shown in equation 2.4.

$$\hat{\boldsymbol{Q}}_{f_k} = [\hat{\boldsymbol{q}}_k^{(1)}, \hat{\boldsymbol{q}}_k^{(2)}, ..., \hat{\boldsymbol{q}}_k^{(N_b)}] \in \mathbb{R}^{N \times N_b} \tag{2.4}$$

This allows the weighted cross spectral density tensor, S_{f_k}, at frequency f_k to be written as equation 2.5 where $(\cdot)^*$ denotes the Hermitian transpose.

$$\boldsymbol{S}_{f_k} = \hat{\boldsymbol{Q}}_{f_k} \hat{\boldsymbol{Q}}_{f_k}^* \tag{2.5}$$

From $\boldsymbol{S}_{f_k}$, the SPOD modes of the k^{th} frequency, $\boldsymbol{\Phi}_{f_k}$, can be found as the eigenvectors from equation 2.6.

$$\boldsymbol{S}_{f_k} \boldsymbol{W} \boldsymbol{\Phi}_{f_k} = \boldsymbol{\Phi}_{f_k} \boldsymbol{\Lambda}_{f_k} \tag{2.6}$$

where $\boldsymbol{W}$ is a positive-definite Hermitian matrix that accounts for both the weight $\boldsymbol{W}(x)$ and the numerical quadrature of the integral of the discrete grid.

However, solving this is computationally expensive and it has been shown by Towne *et al.* (2018) that the modes can be recovered by solving the $N_b \times N_b$ eigenvalue problem in equation 2.7.

$$\hat{\boldsymbol{Q}}_{f_k}^* \boldsymbol{W} \hat{\boldsymbol{Q}}_{f_k} \boldsymbol{\Theta}_{f_k} = \boldsymbol{\Theta}_{f_k} \tilde{\boldsymbol{\Lambda}}_{f_k} \tag{2.7}$$

The non-zero eigenvalues of equation 2.6 are recovered and indicated by $\tilde{(\cdot)}$. By projecting the Fourier coefficients, $\hat{\boldsymbol{Q}}_{f_k}$, onto the new eigenvectors, $\tilde{\boldsymbol{\Theta}}_{f_k}$, as shown in equation 2.8, the mode shapes are obtained exactly.

$$\tilde{\boldsymbol{\Phi}}_{f_k} = \hat{\boldsymbol{Q}}_{f_k} \tilde{\boldsymbol{\Theta}}_{f_k} \tilde{\boldsymbol{\Lambda}}_{f_k}^{-1/2} \tag{2.8}$$

The modes ($\tilde{\boldsymbol{\Phi}}_{f_k}$) are ranked in order of intensity by their eigenvalues in equation 2.9. As shown in Venning *et al.* (2018*a*), the first mode of each frequency, $\phi_{f_k}^{(1)}$, is the most indicative of the 'mean' flow state and as such will be the only modes presented throughout the paper.

$$\tilde{\boldsymbol{\Phi}}_{f_k} = [\phi_{f_k}^{(1)}, \phi_{f_k}^{(2)}, ..., \phi_{f_k}^{(N_b)}] \tag{2.9}$$

This information gives insight into the excitation spectra induced by the cloud cavitation and can be compared to the response spectra to aid in identifying certain components such as cloud cavitation induced force fluctuations and structural natural frequencies. Intensity maps are generated through colour-scaled plots where the intensity level of each pixel is proportional to the intensity level of the corresponding frequency. This provides spatial information revealing the distribution across the image of the shedding modes. By plotting the phase of the Fourier coefficients across the domain, insight into shedding cycle behaviour and interaction between events across the hydrofoil may be gained.

Spatio-temporal information of the cavitation behaviour is also represented through the use of space-time plots. These plots are generated by extracting either the same row or column of pixels from each frame and placing them sequentially next to one another, producing chordwise and spanwise space-time plots, respectively. Interpretation of these plots are discussed in detail by Smith *et al.* (2019).

3. Results & Discussion

As σ is progressively reduced beyond inception the hydrofoil experiences various forms of cavitation. The extent of the cavitation varies from short partial sheet cavities through to supercavitation (Franc & Michel 2004). The characteristics of each regime vary in appearance and an overview of the various regimes is presented in figure 5. Traits are observed to not only vary between each of the cavitation regimes, but also within the regimes themselves. Characterising the cavitating behaviour and the corresponding influence on the hydrofoils performance is achieved by establishing correlations between the measured forces and deflections with the cavitation behaviour observed in the high-speed photography. For the σ range tested, three primary cavitation modes experienced by the hydrofoil were identified which varied in both the mechanism driving shedding as well as the location on the hydrofoil. These cavitation modes are summarized in table 3 as well as indicated on the spectrograms in figure 8.

3.1. *Cavity Length*

The length of the attached cavity was measured for each σ with the cavity length, L_c, taken as the furthest downstream extent of the cavity while remaining attached. When shedding is present, this is the cavity extent in each cycle prior to the shedding event. Cavity lengths were obtained at 4 spanwise positions from chordwise space-time diagrams extracted from the long-duration videos as an average from at least 50 cavity growth/shedding cycles.

The presence and extent of an attached cavity influences the pressure distribution over the hydrofoil and therefore the forces that result. In cloud cavitation conditions, the attached part of the cavity limits the minimum pressure on the suction side to the vapour pressure of the water (Franc 2001). Figure 6 shows the maximum attached cavity length, L_c normalized by the local chord, c, as a function of σ and spanwise position. For $0.4 \leqslant \sigma \leqslant 0.6$, the cavity length exhibits a reduction in the rate of increase with reducing σ compared to higher σ ranges. This reduction in cavity-length growth rate corresponds to the attached cavity reaching the trailing-edge, i.e. $L_c/c = 1.0$. At this stage of development the cavity closure will now directly interact with the flow from the pressure side of the foil, possibly causing the rate of growth to reduce. When σ is reduced

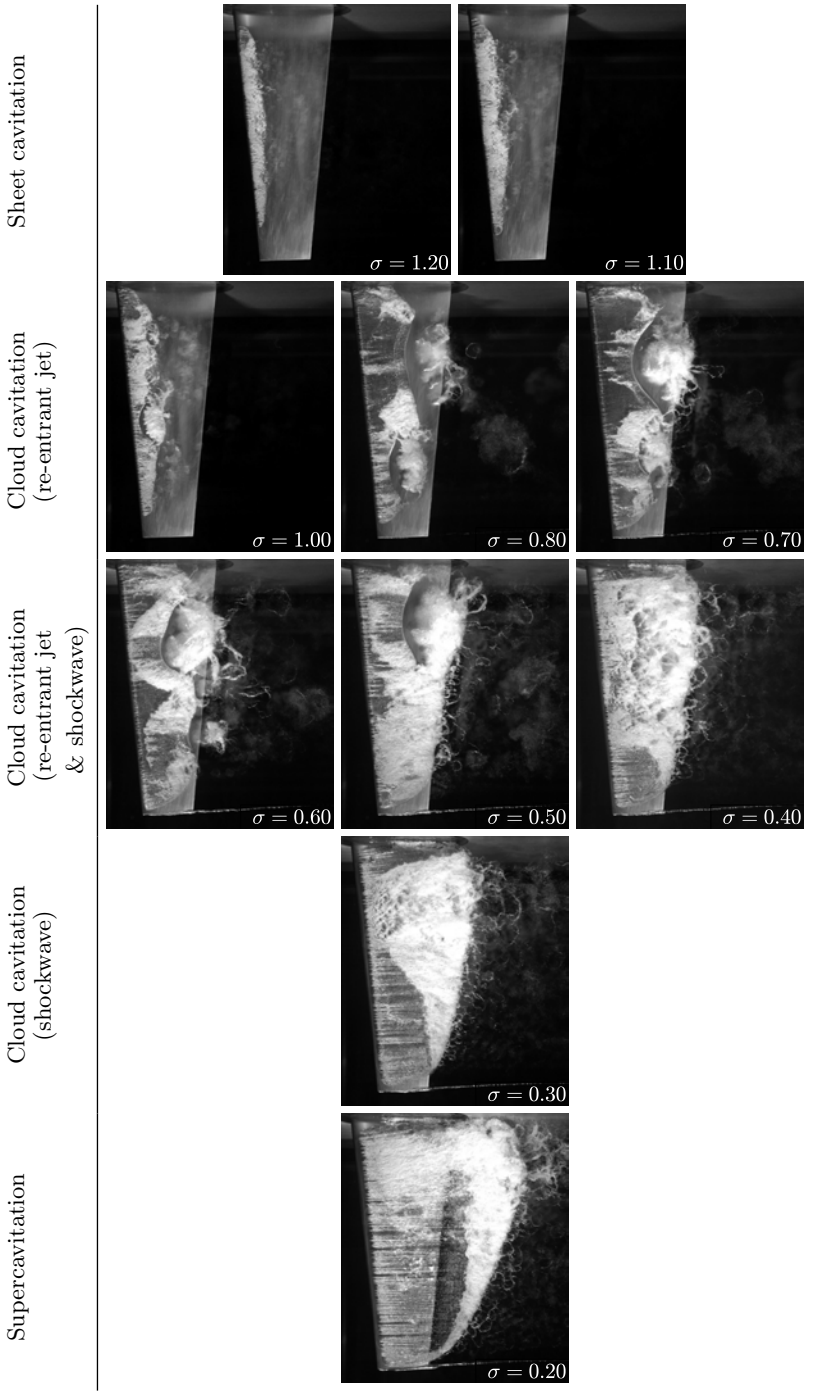

FIGURE 5. Photographs of the hydrofoil with different cavitation regimes through the range of σ below inception. The hydrofoil first experiences stable sheet cavitation ($1.1 \leqslant \sigma < 1.2$), with development of re-entrant jet driven cloud cavitation as σ is reduced ($0.4 \leqslant \sigma \leqslant 1.0$). A further reduction in σ, with cavity length extending to the trailing-edge, upstream propagating condensation shockwaves become the dominant mechanism for shedding ($0.3 \leqslant \sigma < 0.4$). For $\sigma < 0.3$, the cavity envelopes the hydrofoil (supercavitation) and the break-up region is downstream of the trailing-edge.

Cavitation Mode	Mechanism	σ
Type I	Shockwave	0.3 – 0.6
Type IIa	Re-entrant jet (root/tip)	0.4 – 1.0
Type IIb	Re-entrant jet (tip)	0.7 – 0.9

TABLE 3. Summary of the cavitation modes experienced by the hydrofoil for the σ range tested. As σ is reduced from 1.2, the hydrofoil first starts experiencing the re-entrant driven Type IIa mode at $\sigma = 1.0$ with the Type IIb becoming active shortly after at $\sigma = 0.9$. Further reduction in σ sees the disappearance of the Type IIb mode below 0.7 with the shockwave driven Type I becoming active at $\sigma = 0.6$. The Type IIa mode remains active along with the Type I mode down to $\sigma = 0.4$ before disappearing, resulting solely shockwave driven shedding at $\sigma = 0.3$. Supercavitation is reached at $\sigma = 0.2$ where no cavitation modes are active.

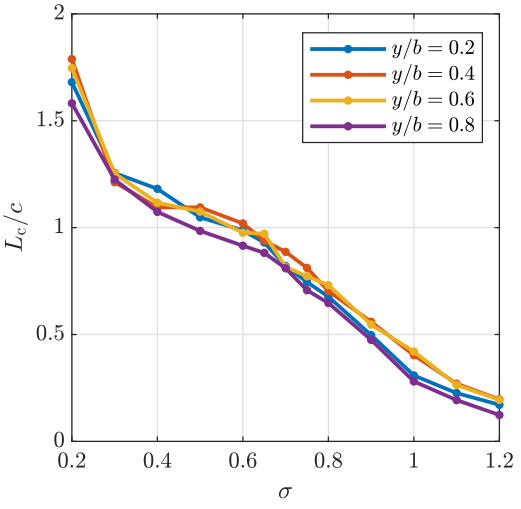

FIGURE 6. Maximum attached cavity length, L_c, as a function of σ, for four spanwise positions. The cavity length is the average length at cavity break-off, and is non-dimensionalised by the local chord, c, at each position. The cavity growth is continuous as σ is reduced.

to 0.2 the cavity length increases to well beyond the local chord, indicating the cavity closure is away from the trailing-edge and hence is in the supercavitating regime.

3.2. *Steady & unsteady components of the forces & deflections*

The mean and standard deviation of the normal force (C_N) and pitching moment (C_P) loads provide insight into the impact of the cavitation on the hydrofoil in terms of both the steady and unsteady forces. Spatial information is obtained through the centre of pressure, x_{cop}, which gives the centre of action of the forces acting along the hydrofoil and is calculated as C_P/C_N and presented as a ratio of the mean chord, $x_{cop}/\bar{c}$, from the leading edge at the root. The non-dimensional tip displacement, $\delta/\bar{c}$, is presented to assess the level of structural response resulting from the hydrodynamic loading.

The mean and standard deviation of C_N, C_P, $x_{cop}/\bar{c}$ and $\delta/\bar{c}$ are shown in figure 7 as functions of σ, with $'$ denoting the standard deviation of the time-varying quantities. As σ is decreased from 1.2 to 1.1 (sheet cavitation regime, see figure 5), all standard deviations increase despite little change in the mean load and displacement. Further reduction in σ

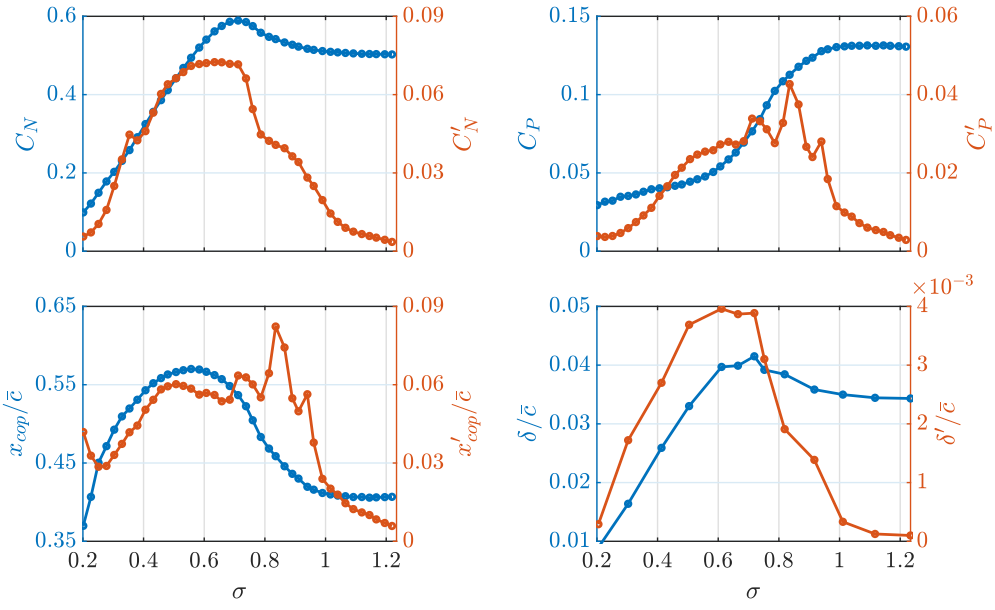

FIGURE 7. Mean (blue) and standard deviation (orange) of the normal force (C_N), pitching moment (C_P), location of the centre of pressure ($x_{cop}/\bar{c}$) and tip displacement ($\delta/\bar{c}$) at various σ where $'$ indicates the standard deviation of the time varying quantity. The results show the effect of various cavitation regimes revealing unique characteristics in the steady and unsteady components.

to 1.0 sees a significant change in the unsteady loading with C'_N approximately doubling and is attributed to the transition to the cloud cavitation regime with re-entrant jet driven shedding at $\sigma \approx 1.0$. This increased unsteadiness is attributed to the increased volume of the shedding clouds associated with re-entrant jet driven shedding compared to sheet cavitation having greater impact on the hydrofoils pressure distribution.

Initially as σ is reduced into the cloud cavitation regime ($0.3 \leqslant \sigma \leqslant 1.0$), C_N continues to increase, reaching a maximum at $\sigma = 0.71$, corresponding with the maxima in C'_N, $\delta/\bar{c}$ and $\delta'/\bar{c}$. This is attributed to the increase in effective camber of the cavitating hydrofoil due to the presence of the cavity and is discussed further in §3.4.2. There is a marked increase in C'_N and $\delta'/\bar{c}$ for $\sigma = 0.8$ to 0.7 which is associated with the lock-in phenomena discussed later in §3.4.3. Further reduction in σ below 0.7 sees a steady decrease in C_N and C'_N with the mean normal force reducing monotonically into the supercavitating regime.

Despite C_N initially increasing with reducing σ, C_P decreases with the onset of unsteady shedding, dropping more sharply as σ is reduced from 1.0 to 0.7. This is due to the growing cavity shifting the x_{cop} towards mid-chord, reducing the lever arm of the applied load. The rate C_P decreases is reduced as the cavity approaches the trailing-edge at $\sigma \approx 0.6$ with $x_{cop}/\bar{c}$ reaching a maximum of 0.57 at $\sigma = 0.56$. Interestingly, x_{cop} starts moving back towards the leading edge as σ drops further despite the cavity covering the entire chord as the pressure field varies around the combined hydrofoil/growing cavity system. The displacement and normal force measurements, both mean and standard deviation, exhibit similar trends, indicating a strong correlation between the two as expected. A strong correlation is also observed between x'_{cop} and C'_P.

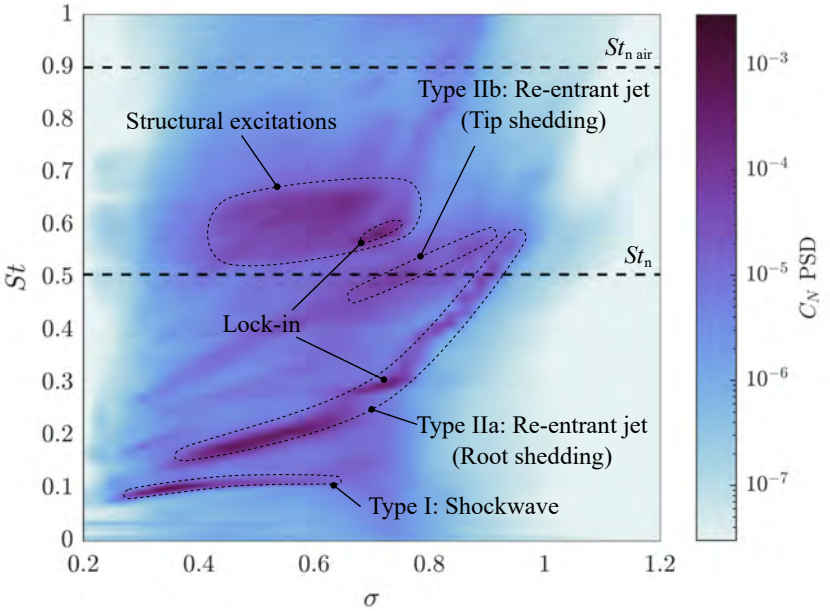

FIGURE 8. Spectrogram of the normal force for a range of σ showing the global unsteady behaviour. The results highlight the shockwave driven Type I shedding frequency is predominantly independent of σ while the re-entrant jet driven Type IIa & IIb shedding modes are highly dependant on σ. The natural frequency of the hydrofoil in-air, $St_{\text{n air}}$, and fully wetted, St_{n}, are indicated by two horizontal dashed lines.

3.3. *Forces & Deflections Spectra*

The amplitude and frequency content of the forces acting on the hydrofoil is dependent on multiple factors including hydrodynamic loading, cavitation dynamics and the structural response. A spectrogram of C_N for varying σ (figure 8) provides a global perspective of how the cavitation behaviour modulates the spectral characteristics. The spectrogram is constructed from spectra of the long-duration measurements at 0.025 increments of σ. Spectra of C_N were obtained using the Power Spectral Density (PSD) derived with the Welch estimate (Welch 1967) utilizing a Hanning window with size and overlap of 2 048 (2.05 s) and 512 (0.51 s) samples, respectively, on the 360 000 (360 s) sample time series. Frequency is non-dimensionalized as a chord-based Strouhal number, $St = fc/U_\infty$. Individual spectra plots at σ values of particular interest are presented in figure 9 along with the corresponding tip deflection spectra calculated from the medium duration time series data.

There are 3 primary modes identified in the spectra which are referred to as Types I, IIa and IIb in the text. The Type I mode is associated with shockwave-driven periodic shedding occurring along a majority of the span with the shedding frequency observed to be essentially independent of σ. The Type IIa & IIb modes are both driven by a re-entrant jet instability and are dependant on σ. Type IIa 'root shedding' events occur at various spanwise positions depending on σ, while Type IIb 'tip shedding' events are confined to the lower portion ($0.5 < y/b < 1.0$). This nomenclature follows that used by Kjeldsen & Arndt (2001) where shockwave and re-entrant jet type shedding mechanisms were termed

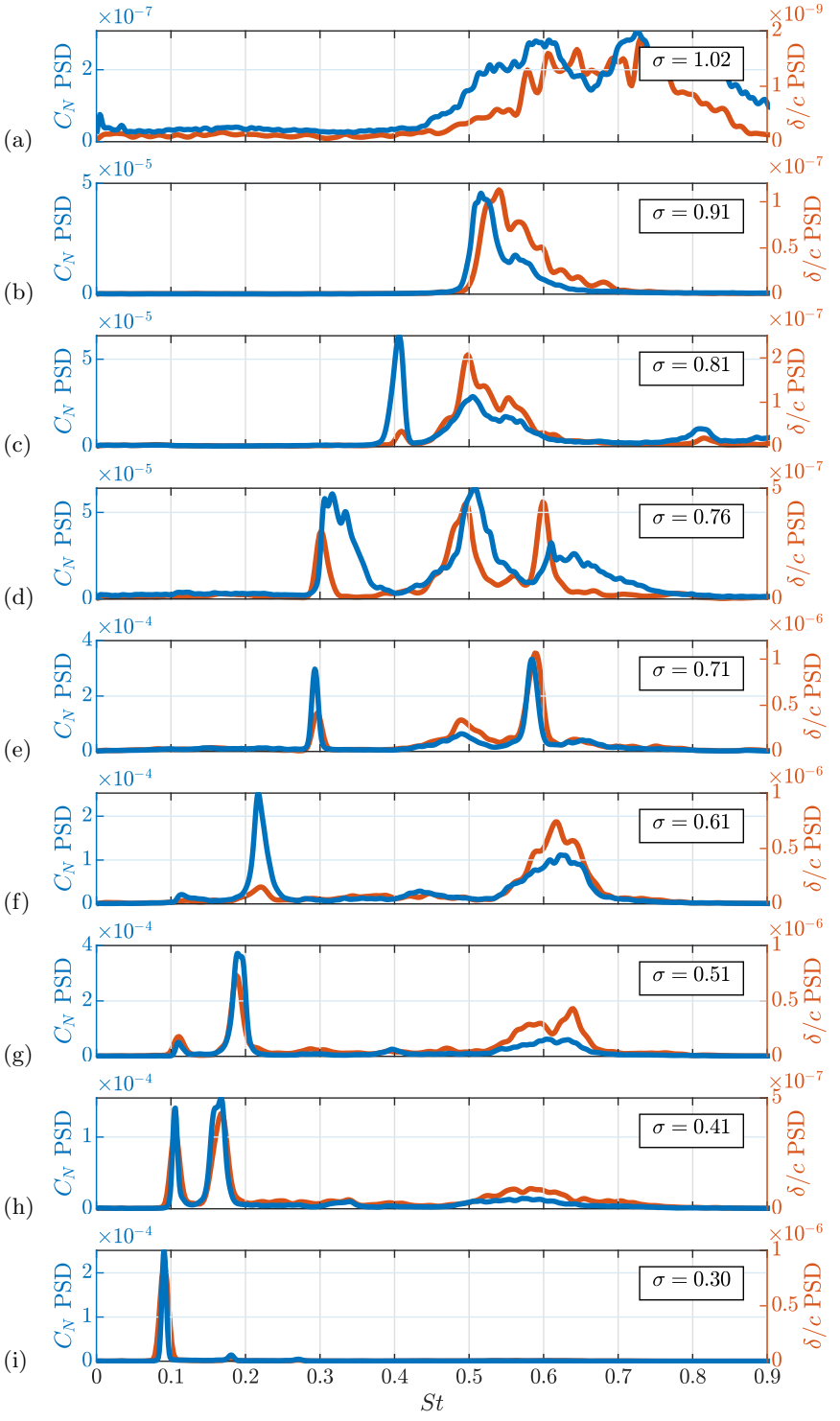

FIGURE 9. PSD of the normal force (blue) and tip displacement (orange) time series at selected σ. The various spectra show the peak frequencies shift as σ varies with both the normal force and tip displacement exhibiting similar spectral characteristics across the selected σ values. Note that the vertical scales vary (by orders of magnitude) between the plots.

Types I and II, respectively. The analysis undertaken to identify these various modes is described in §3.4.

As previously observed with both 2D (Kawanami *et al.* 1998; Prothin *et al.* 2016) and 3D geometries (Smith *et al.* 2018), the cavitation pattern over a hydrofoil varies with σ, such as shedding sites, cavity length and cavitation cloud size. The frequency at which these shedding events occurs is also dependant on their spanwise location, particularly in the present case of finite and spanwise varying geometry. Utilizing the intenisty maps from the SPOD (figure 10) applied to the high-speed photography provides spatial information with respect to the cloud cavitation regime to qualitatively identify periodic shedding sites at each σ. Used in conjunction with the C_N and $\delta/\bar{c}$ response spectra, the intensity and phase maps allow modes evident in the response spectra to be attributed to associated cavity dynamics.

Within the stable sheet cavitation regime ($\sigma \geqslant 1.1$), there is little unsteady content in C_N with no tonal peaks observed in the spectra (not shown in figure 9). Once σ is reduced below 1.1, with cloud cavitation forming, fluctuations in both C_N and $\delta/\bar{c}$ are now significant (increasing by two orders of magnitude between $\sigma = 1.02$ and 0.91) with distinct tonal peaks becoming apparent (figure 9b). Two distinct peaks are evident in the C_N and $\delta/\bar{c}$ spectra at $\sigma = 0.91$, both of which decrease in frequency as σ is reduced to 0.81 (figures 9b & 9c). These peaks are associated with the formation of two shedding sites along the span of the hydrofoil discussed later in §3.4.2. The shedding at these two sites are referred to as Type IIa and Type IIb oscillations for the root and the tip, respectively.

A shift in the peak frequency occurs in conjunction with the appearance of a third peak in the spectra at $\sigma = 0.76$ as σ is reduced below 0.8 (figure 9d). The C_N spectrogram (figure 8) shows the Type IIa frequency jumping down to $St = 0.31$ and increasing in magnitude with an intense peak appearing at double the frequency ($St = 0.61$) for $0.7 \leqslant \sigma \leqslant 0.76$. This feature is attributed to lock-in where the Type IIa shedding frequency has transitioned to match a sub-harmonic of the hydrofoils first bending mode (f_n). As given in table 1, the hydrofoil first bending mode occurs at 55 Hz ($St_n = 0.52$) in fully wetted conditions, which is lower than the third peak at $St = 0.61$. This difference in frequency is attributed to the presence of the vapour cavity reducing the added mass and causing frequency modulation. The Type IIb peak continues a steady decrease to $St = 0.51$ at $\sigma = 0.76$ (figure 9d).

Lock-in is also apparent in the tip displacement spectrum at $\sigma = 0.7$ (figure 9e) in the appearance of the third peak along with amplification of the Type IIa spectral peak (also reflected in the increase in δ'/c shown in figure 7). As σ is reduced below 0.65, the hydrofoil comes out of lock-in with the Type IIa oscillations dropping to $St = 0.22$, the Type IIb mode fading out and significant broadband excitation in C_N and $\delta/\bar{c}$ appearing at $St \approx 0.62$ (see figure 9f) attributed to structural excitations.

The Type IIa shedding frequency continues to steadily decrease as the attached cavity length grows, showing a linear dependence on σ until it disappears at $\sigma \approx 0.4$. The spectra also shows the emergence of an additional frequency at $St = 0.11$ for $\sigma \lessapprox 0.6$ that is nominally independent of σ. The appearance of this new feature coincides with the cavity reaching the trailing-edge (figure 6) and is attributable to the presence of the shockwave instability (Type I). In addition, the broadband excitation appearing at $St \approx 0.62$ is linked to structural excitations outside of lock-in conditions, apparent down to $\sigma = 0.4$. Type I and IIa instabilities are both present from $\sigma = 0.6$ down to 0.4 with the Type I amplitude increasing as σ is reduced.

Once σ is reduced below 0.4, only the Type I mode remains with $St \approx 0.09$ oscillations dominant, as shown in figure 9i. As also observed by Kjeldsen *et al.* (2000) and Smith *et al.*

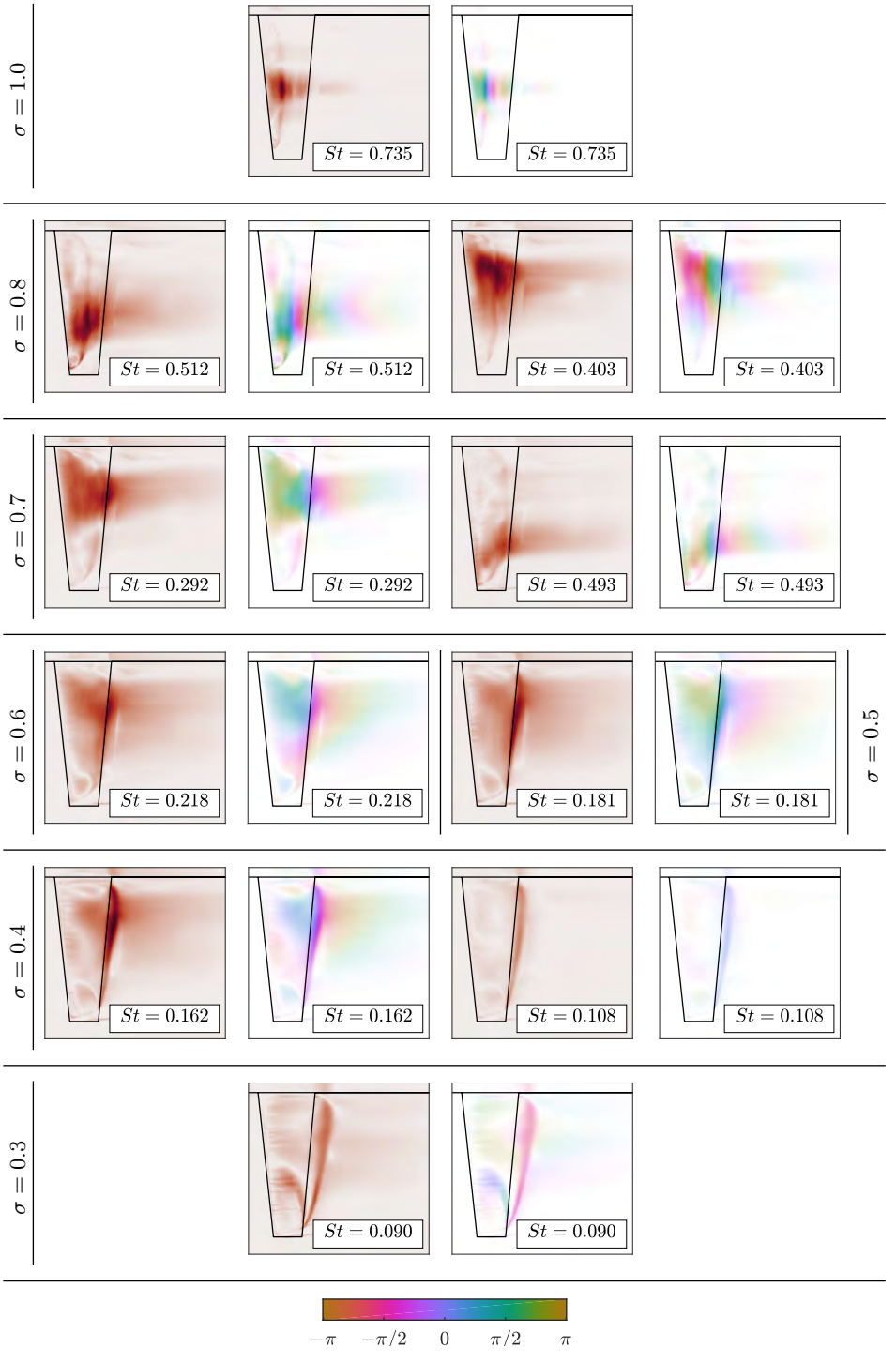

FIGURE 10. Spectral POD intensity (red) and phase maps (coloured) of key modes for various σ highlighting regions of high activity at the frequencies of interest. The color intensity distribution in each phase map is directly proportional to that of the corresponding intensity map. The spectral and spatial information aids in the identification of the mechanisms driving oscillations with phase maps providing the relative timing of each cycle.

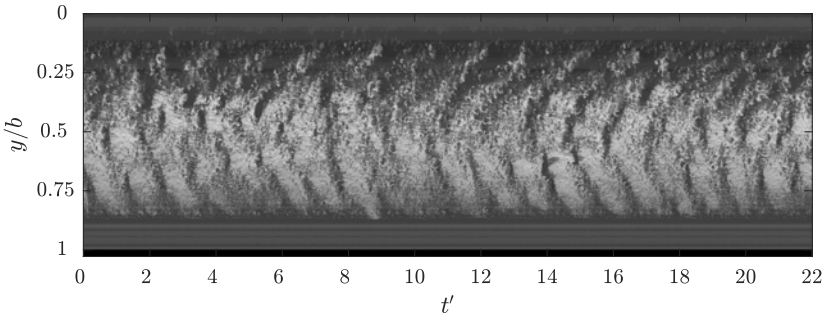

FIGURE 11. Spanwise space-time plot taken at $x/c_{\text{root}} = 0.35$ shows the shedding small-scale vapour structures along the span due interfacial instabilities for $\sigma = 1.1$. While there is evidence of periodic break-up, the influence on the forces and deflections are minimal.

(2018), the Type I mode shows little to no dependence on σ, however, Kawakami *et al.* (2008) found this only to be valid for cases with relatively high gas content (~ 13 ppm), which was not the condition in the present study.

The shockwave-driven Type I mode is no longer apparent in the supercavitating regime ($\sigma = 0.2$). The C_N spectrogram (figure 8) reveals minimal excitations with no tonal peaks for $\sigma = 0.2$. All associated cavity dynamics with observations made in the forces and deflections for each cavitation regime will be discussed in §3.4.

3.4. *Cavity Dynamics*

3.4.1. *Sheet Cavitation*

Sheet cavitation occurs at relatively high σ ($1.1 \leqslant \sigma \leqslant 1.2$) and is confined to a small portion of the chord towards the leading edge (supplementary movie 1). The space-time plot taken at $x/c_{\text{root}} = 0.35$ (figure 11) shows coherent shedding of small-scale vapour structures. However, the cavity at the extreme extents (not shown in the space-time) is stabilised by the re-entrant jet at the tip and the tunnel ceiling boundary layer at the root. Cavity break-up is driven primarily by interfacial instabilities such as Kelvin-Helmholz driven spanwise vorticity lines (Avellan *et al.* 1988) and turbulent transition (Brennen 1995). Some recent investigations have observed this phenomena in cavitating flows about a rectangular planform finite-span hydrofoil (Russell *et al.* 2018) and about a sphere (Brandner *et al.* 2010; de Graaf *et al.* 2017). The shedding of these small-scale structures only cause minimal broadband force fluctuations as they are not large enough to cause any significant changes in the flow over the hydrofoil and hence, unsteadiness in the pressure distribution and resulting developed forces.

As σ is reduced, the cavity grows into a region of an increasingly adverse pressure gradient, a re-entrant jet begins to form extending upstream along the hydrofoil surface. For the re-entrant jet to act as a mechanism for cavity break-up and cloud shedding it needs to reach the upstream extent of the cavity (Pelz *et al.* 2017). This will only occur in practice if the cavity is sufficiently thick (Franc 2001). Note that for a given flow configuration the cavity thickness will increase in proportion to the length. As observed by Callenaere *et al.* (2001), a relatively thin cavity is highly susceptible to the interfacial instabilities of both interfaces (i.e. re-entrant jet/cavity surface) interacting, leading to break-up of the cavity into small-scale vapour structures, rather than the re-entrant jet progressing sufficiently upstream to act as a mechanism for the cloud instability. As shown in figure 5, the conditions to satisfy these requirements for cloud shedding to form are reached by $\sigma = 1.0$.

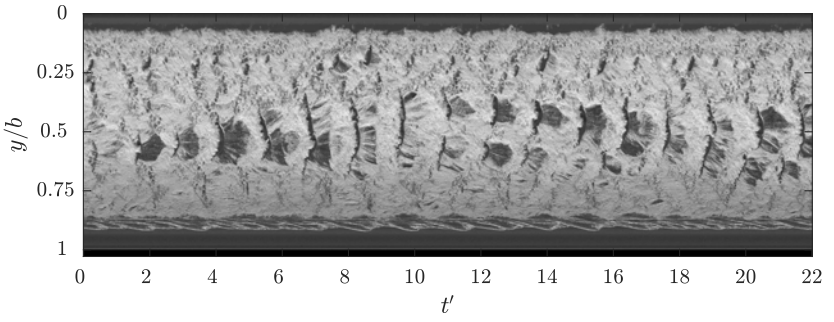

FIGURE 12. Spanwise space-time plot taken at $x/c_{\text{root}} = 0.31$ for $\sigma = 1.0$ shows the re-entrant jet instability around mid-span causing periodic shedding with its spatial distribution varying through time.

3.4.2. *Re-entrant jet driven shedding (pre-lock-in)*

Cloud cavitation occurs when σ is reduced to 1.0 with the conditions allowing the re-entrant jet to reach the upstream extent of the attached cavity, causing periodic detachment and the formation of a cavitation cloud. As shown by the space-time plot in figure 12 (supplementary movie 2), re-entrant jet driven shedding only occurs around mid-span with the detachment of small bubbly vortices occurring towards the spanwise extents. This behaviour is also evident in the intensity maps for $\sigma = 1.0$ at $St = 0.74$ (figure 10). This is due to the three-dimensionality of the geometry with localised tip flow introducing a spanwise velocity component that locally prevents the re-entrant jet reaching the leading edge.

Likewise, the ceiling boundary layer modifies the local pressure distribution and streamwise velocity component in the vicinity of the root, adversely affecting formation of the re-entrant jet in the region. This results in areas of stable cavities at the spanwise extents of the attached cavity, as seen in figure 5. The shedding of cavitation clouds at $\sigma = 1.0$ induces relatively low force fluctuations, as indicated by C'_N (figure 7), at a frequency around $St \approx 0.70$ (evident also in the C_N spectra (figure 9) and space-time plot (figure 12)). The shedding frequency is relatively broadband and can be attributed to the varying spanwise shedding location seen in the space-time plot, where the varying cavity length changes the duration for the re-entrant jet to reach the leading edge, thus broadening the shedding frequencies present in the spectra. It is also apparent that the changing shedding location doesn't move randomly, but is dependant on the previous cycle. This is due to the spanwise component of the previous cycle's re-entrant jet preventing other instabilities from interfering in the next shedding cycle at that spanwise location (de Lange & de Bruin 1998).

As σ is decreased further to 0.9, the cavity size increases along with the re-entrant jet thickness (Callenaere *et al.* 2001), giving it the momentum to overcome spanwise flow components and reach the leading edge for the majority of the span. The increased cavity length and inherent cavity dynamics results in a spatial compatibility with the span, resulting in the formation of two re-entrant driven shedding modes (Type IIa & IIb). The increased cavity size results in significant excitation in C_N and $\delta/\bar{c}$ and by $\sigma = 0.8$ two tonal frequencies become evident in the spectra (figure 9) at $St = 0.41$ and 0.50, corresponding to multiple shedding sites along the span (figure 10). As noted previously, the frequency of these modes decreases with σ which is due to the re-entrant jet requiring more time to break through the attached cavity as it has more distance to travel upstream (as cavity length grows) with decreasing σ (figure 6).

The Type IIa & IIb shedding modes occur towards the root and tip, respectively,

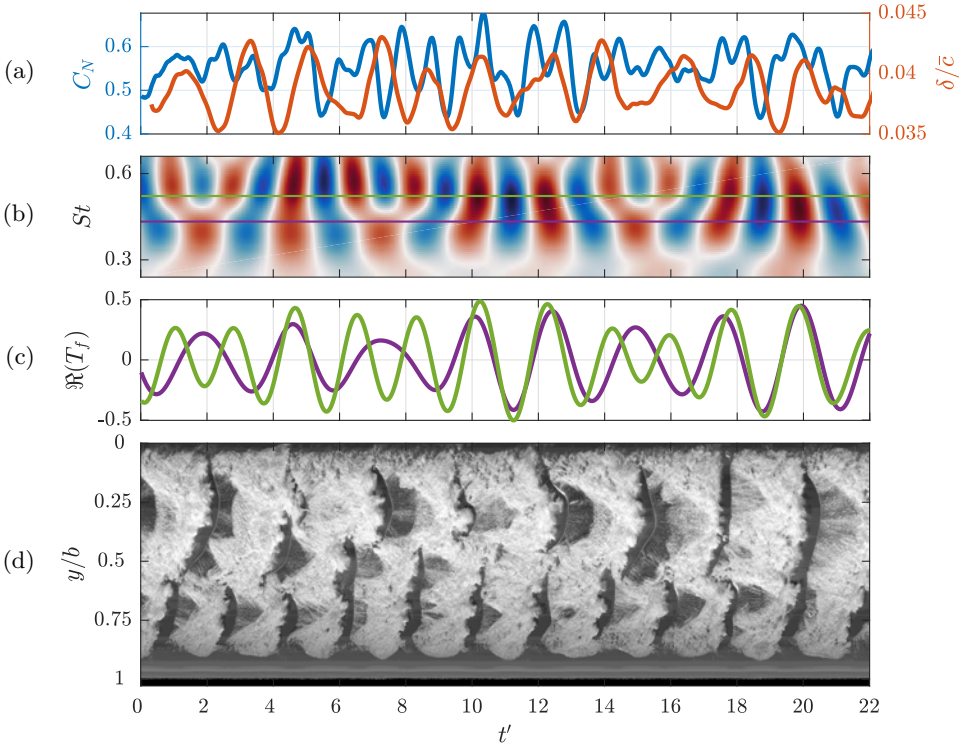

FIGURE 13. Synchronised time series of the normal force (C_N) and the tip displacement ($\delta/\bar{c}$) (a) at $\sigma = 0.8$ with the real value of the C_N Morlet wavelet transform (b). The $St = 0.41$ (purple) and 0.50 (green) components of the wavelet transform (c) show the connection between the C_N fluctuations and the Type IIa and IIb shedding events evident in the spanwise space-time plot taken at $x/c_{\text{root}} = 0.5$ (d).

and are evident in the space-time plot in figure 13d and supplementary movie 3 where the shedding frequencies match those in the C_N and $\delta/\bar{c}$ spectra. SPOD intenisty and phase maps of the cavitation behaviour at $\sigma = 0.8$ (figure 10) show the Type IIa activity ($St = 0.41$) is confined to the upper portion of the span ($0.0 < y/b < 0.4$), with the Type IIb activity ($St = 0.50$) focused to the lower portion ($0.6 < y/b < 0.8$). Additionally, the wavelet transform of C_N in figure 13 shows two primary frequencies occurring simultaneously and are always present over time. Comparing extracted wavelet components at $St = 0.41$ and 0.50 with the spanwise space-time plot reveals a strong correspondence with the Type IIa and Type IIb shedding events (figure 13).

The C_N spectrum at $\sigma = 0.8$ reveals that the $St = 0.41$ amplitude is greater than that at $St = 0.50$, where the opposite is true in the $\delta/\bar{c}$ spectra with $St = 0.50$ exhibiting the greater amplitude. This is attributed to the Type IIa shedding events being of greater magnitude from a longer cavity with the larger local chord, thus having more influence on C_N. For the Type IIb shedding events, they occur towards the tip and despite their reduced magnitude, the shedding events have more influence on the tip displacement due to the increased lever of the resulting force acting on the cantilevered hydrofoil. Hence, the spatial distribution of the cloud cavitation influences the C_N and $\delta/\bar{c}$ spectra.

As the cavity grows with the reduction in σ, it changes the flow over the suction side of the hydrofoil. The presence of the cavity increases the effective camber of the hydrofoil and therefore increasing the lift force (Young *et al.* 2018), despite minimum pressure limitations imposed by the cavity. This results in a steady increase in the mean C_N as σ

is reduced, reaching a maximum at $\sigma = 0.7$ (figure 7). The resulting pressure distribution also becomes sensitive to cavitation clouds being advected along the chord, contributing to the rise in C'_N which reaches a maximum at a point coinciding with the maximum C_N. With further reduction in σ from 0.7, both C_N and C'_N decrease as the minimum pressure limitation imposed by the cavity becomes more influential than the increased flow curvature.

The presence of the attached cavity significantly alters the pressure distribution over the suction side of the hydrofoil compared to the fully wetted case (Leroux *et al.* 2004). The cavity imposes a minimum pressure limitation equal to p_{v} where the vapour filled cavity is attached to the surface, reducing the mean load on the hydrofoil (Franc 2001). Additionally, the presence of the cavity modifies the streamlines over the hydrofoil having the effect of either increasing or decreasing the effective camber (Young *et al.* 2018). The increase in the mean C_N as σ is reduced to 0.7 (figure 7) is attributed to the increase in effective camber of the cavitating hydrofoil. As σ is reduced below 0.7, the cavity growth now alters the flow over the suction side that results in a decrease in effective camber, reducing the loading on the hydrofoil.

3.4.3. *Lock-in*

The lock-in phenomena occurs when when a structure is being excited by an instability of which its frequency will deviate to match with a relatively close structural natural frequency, resulting in significant amplification of the structural response. This has previously been observed in hydrofoil's experiencing cloud cavitation (Akcabay & Young 2014; Akcabay *et al.* 2014; Pearce *et al.* 2017; Harwood *et al.* 2019*a*,*b*) with Akcabay & Young (2015) showing that parametric excitations cause frequency modulation in the vibration response. This is due to changes in the fluid-mixture density causing fluctuations in effective fluid-added mass.

As σ is reduced below 0.8, both the Type IIa & IIb shedding frequencies decrease due to the increasing cavity length until σ reaches 0.75. The reduction in shedding frequency leads to the hydrofoil experiencing lock-in for $0.65 \leqslant \sigma \leqslant 0.75$. Lock-in occurs as the excitation frequency from the periodic shedding falls into a finite band surrounding a resonance of the hydrofoil, forcing it to lock-in to the natural frequency, leading to amplification of small motions and fluctuating fluid loads (Harwood *et al.* 2019*a*). This is observed to occur on the current hydrofoil where the Type IIa excitation shedding frequency matches a sub-multiple of the hydrofoil natural frequency with an additional peak appearing in the spectra at twice the frequency. This third spectral is associated with the first bending mode of the hydrofoil which has been modulated due to the presence of the vapour cavity. With a portion of the hydrofoil oscillating in vapour instead of liquid, the added or entrained mass, along with the hydrodynamic stiffness is reduced (De La Torre *et al.* 2013; Harwood *et al.* 2019*a*,*b*), increasing the natural frequency to $St \approx 0.61$. Hence, as the Type IIa shedding mode approaches the first sub-harmonic ($f_{\mathrm{n}}/2$) of the hydrofoils first bending mode, the frequency deviates to lock-in to the structural excitations and causing excitations at $St = 0.61$ (structural) & $St = 0.31$ (cavity driven).

Lock-in causes the Type IIa mode to reduce to a shedding frequency of $St = 0.29$ at $\sigma = 0.7$, evident in the space-time plot in figure 14. The SPOD intensity map (figure 10) shows the Type IIa mode occupying a greater portion of the span compared to $\sigma = 0.8$, extending further towards the tip. This has resulted in a shift towards the tip for the Type IIb mode ($St = 0.49$), as well as a reduction in its area of influence shown in supplementary movie 4.

The Type IIb mode doesn't experience any significant frequency modulation, dropping

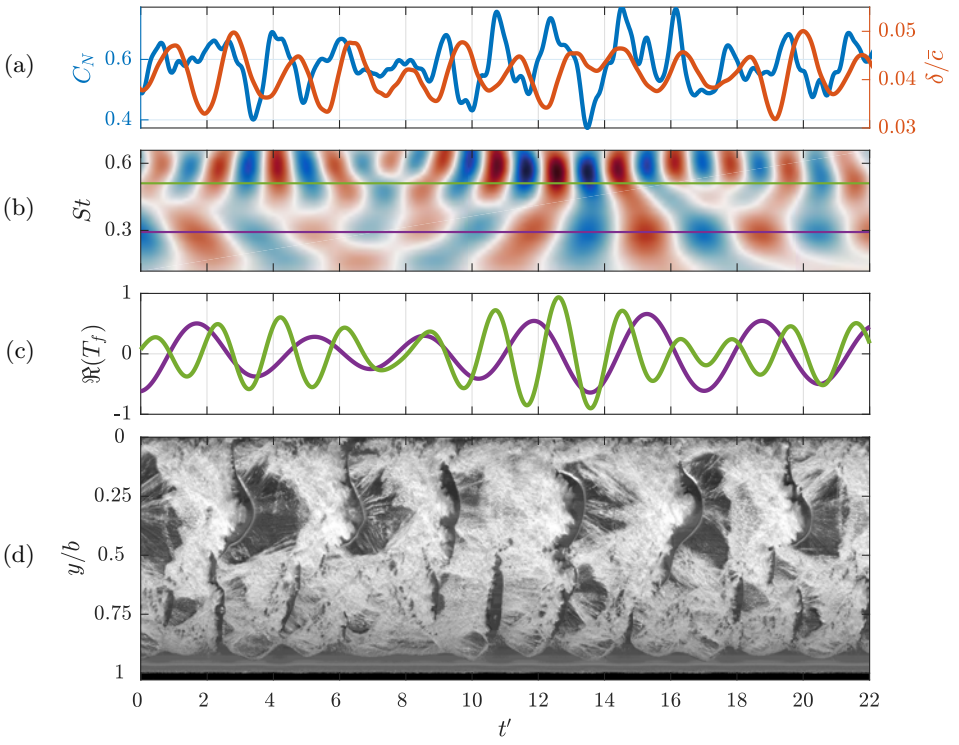

FIGURE 14. Synchronised time series of the normal force (C_N) and tip displacement ($\delta/\bar{c}$) (a) at $\sigma = 0.70$ with the real value of the Morlet wavelet transform for C_N (b) followed by the $St = 0.30$ (Type IIa, green) and 0.488 (Type IIb, purple) components (c). Peaks in the two frequency components are seen to coincide with shedding events in the upper and lower portion of the span as shown in the spanwise space-time plot taken at $x/c_{\text{root}} = 0.5$ (d).

to $St = 0.49$ by $\sigma = 0.7$. However, comparison of the space-time plot (figure 14d) with cases just above and below ($\sigma = 0.8$ and 0.6 in figures 13d and 15c) reveals increased disruption of the cavity dynamics when lock-in is present (i.e. more bubbly appearance) towards the tip is observed as shown in the spanwise space-time diagrams. This may be attributable to the increased tip vibrations preventing stable cavity growth in the region. Besides the minimal additional surface perturbations during lock-in, the lack of frequency modulation suggests the cloud cavitation influences deformations but the deformations are not large enough to influence the primary cloud cavitation behaviour.

3.4.4. *Re-entrant jet and shockwave driven shedding (post lock-in)*

With a sufficient reduction in σ to 0.6, the decrease in cavity shedding frequency from the increased cavity length brings the hydrofoil out of lock-in. From this point, the hydrofoil no longer experiences Type IIb shedding with the C_N and $\delta/\bar{c}$ spectra dominated solely by the Type IIa shedding mode at $\sigma = 0.6$. The increased cavity length and width of the shedding cavitation clouds is no longer compatible with the hydrofoils span to form multiple stable shedding sites. This results in a single periodic shedding site in the upper half of the span, as evident in the space-time plot in figure 15c. In the lower half, the cavity is shed at the same frequency, albeit with less energy (figure 10).

At $\sigma = 0.6$, the attached cavity has reached the trailing-edge with $L_c/c \approx 1.0$ at all spanwise positions (figure 6). Shortly after which the centre of pressure starts shifting back towards the leading edge with further reduction in σ. This is attributed to the

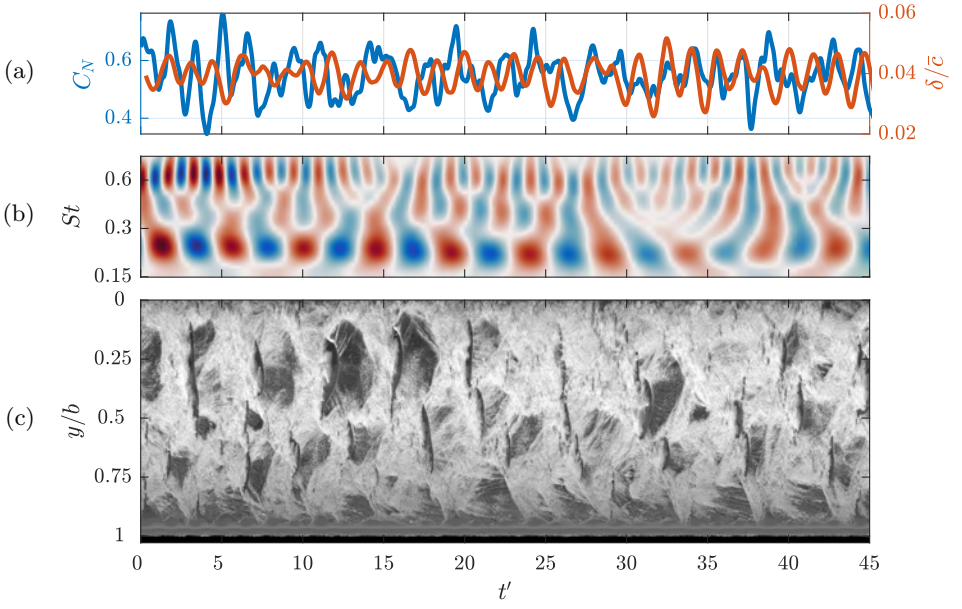

FIGURE 15. Synchronised time series of the normal force (C_N) and tip displacement ($\delta/\bar{c}$) (a) with the real value of the Morlet wavelet transform for C_N (b) at $\sigma = 0.6$. The hydrofoil experiences a relatively consistent $St = 0.22$ oscillation due to the Type IIa shedding as shown in the spanwise space-time plot taken at $x/c_{\text{root}} = 0.5$ (c). Irregular shedding of small-scale structures in the lower half of the span result in inconsistent and varying intensities at higher frequencies evident in the wavelet transform.

suction side increasingly experiencing a uniform p_{v} pressure distribution along the chord due to the attached cavity. This increases the relative contribution of the fully wetted side's pressure distribution, shifting x_{cop} back towards the leading edge, as shown in figure 7.

With the cavity reaching the high-pressure region near the trailing-edge and closing in a region with a low adverse pressure gradient, the shockwave instability becomes active in the flow at low σ. As the cavity grows, the re-entrant jets forms and progresses upstream, slowing down as it approaches the upstream extent of the attached cavity and stalling before it causes the cavity to detach. The re-entrant jet behaviour causes perturbations to form over the attached cavity as it grows with small-scale break-up generating a bubbly flow in the region with a high void fraction, shown in supplementary movie 5. This preconditions the flow for condensation shockwaves to propagate upstream from the collapse of the cavity as it reaches the higher pressure region downstream of the trailing-edge. Preconditioning of the flow allows shockwave propagation to cause the shedding of cloud cavitation where the re-entrant jet instability drives the frequency that the shedding occurs, therefore showing a dependence on σ with frequency dropping linearly with σ (figure 8) .

As σ is reduced to 0.5, the shedding frequency decreases in a linear trend to $St = 0.19$ with induced C_N fluctuations becoming more consistent as evident in the C_N wavelet transforms for $\sigma = 0.6$ and 0.5 in figures 15b and 16b, respectively. This is due to the larger cavity influencing more of the span, as evident in the SPOD intenisty maps of $\sigma = 0.5$ and 0.6 (figure 10). This increased coherent spanwise activity is due to several shedding events (of similar length scale and hence frequency) starting near the root and then occurring successively out along the span. This is shown in the space-time plot

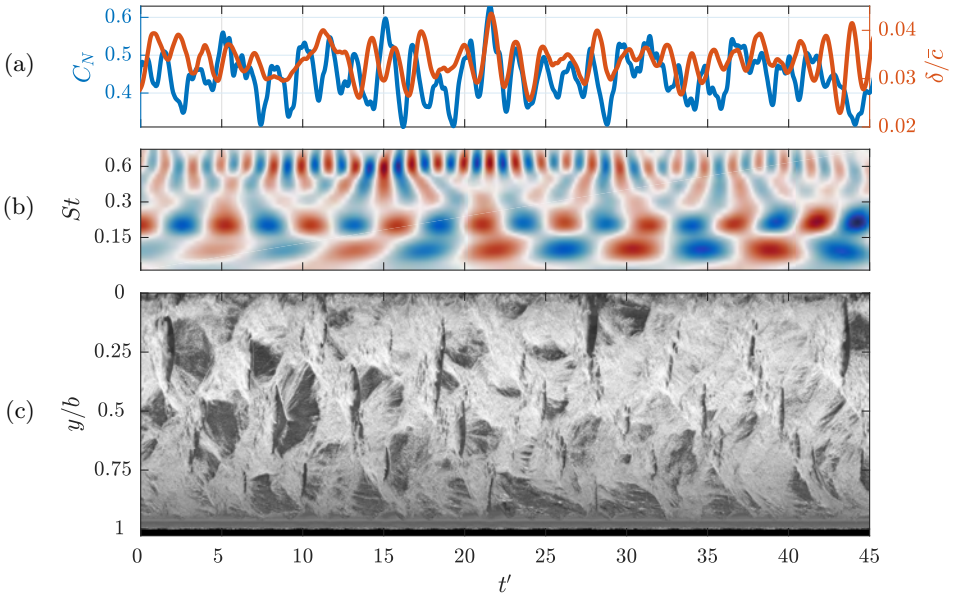

FIGURE 16. Synchronised time series of the normal force (C_N) and tip displacement ($\delta/\bar{c}$) (a) and the real value of the Morlet wavelet transform for C_N (b) at $\sigma = 0.5$. The spanwise space-time plot (c) taken at $x/c_{\text{root}} = 0.5$ reveals multiple shedding events along the span and the complex cavitation behaviour.

(figure 16c) by groups of 3-4 gaps in the cavitation per cycle, starting at the top and moving down in a regular sequence. This is shown to occur 8 times in the space-time plot from $t' = 0$ to 45, resulting in an approximate frequency of 20 Hz, or $St \approx 0.19$, matching the C_N and $\delta/\bar{c}$ spectra.

The Type IIa shedding is apparent down to $\sigma = 0.4$ where the attached cavity extends beyond the hydrofoils trailing-edge before detaching periodically at $St = 0.17$, evident in the C_N and $\delta/\bar{c}$ spectra. Observations from the space-time plot in figure 17c and supplementary movie 6 indicates an alternating shedding behaviour where a cloud is shed from the upper portion of the span ($0.0 < y/b < 0.4$), followed by a cloud from the lower portion. This has manifested in the SPOD intensity and phase maps where two primary energetic areas that appear on the planform are out of phase for $St = 0.16$.

3.4.5. *Shockwave driven shedding*

The onset of shockwave propagation occurs as σ is reduced to 0.6 where the cavity length is now about equal to the chord, $L_c \approx c$, and closes in a relatively weak adverse pressure gradient. The increased size of the attached cavity results in larger cavitation clouds being shed which have a sufficient bubble population and void fraction to permit shockwave formation. This occurs when the cloud is advected downstream of the trailing-edge into a high-pressure region where the cluster of bubbles collapse coherently. The bubbles from the larger cavitation clouds at the reduced σ also increases the local void fraction to the point that the speed of sound in the bubbly mixture reduces significantly compared to that of the constituent water, air and vapour (Shamsborhan *et al.* 2010). This makes the compressible liquid-vapour mixture susceptible to condensation shocks suddenly changing the local void fraction as the shock propagates through the medium (Crespo 1969; Noordzij & Van Wijngaarden 1974; Brennen 2005; Ganesh *et al.* 2016).

The C_N and $\delta/\bar{c}$ spectra show that both Type I & IIa modes are evident for $0.4 \leqslant \sigma \leqslant$

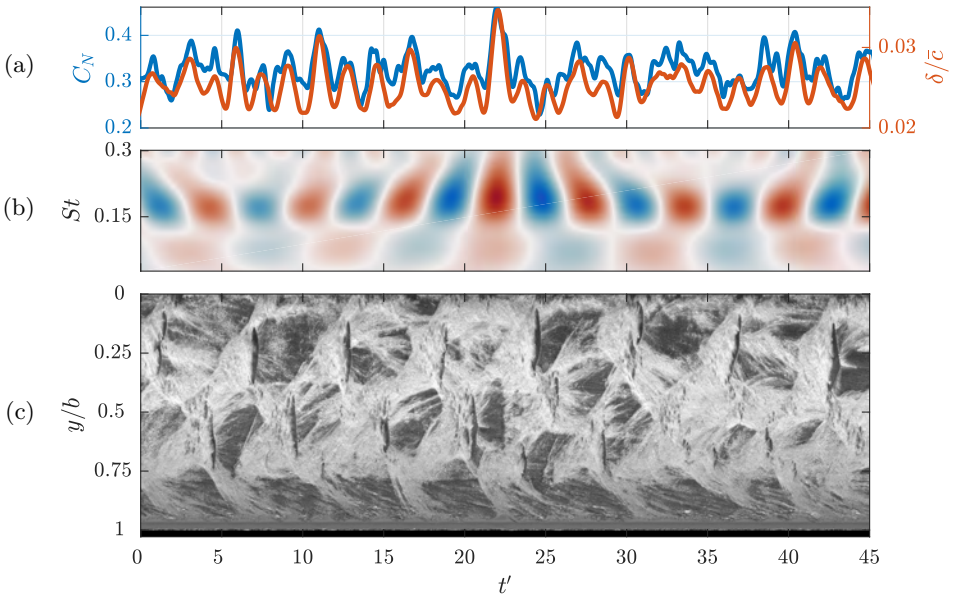

FIGURE 17. Synchronised time series of the normal force (C_N) and tip displacement ($\delta/\bar{c}$) (a) at $\sigma = 0.4$, showing strong correlation, with the real value of the Morlet wavelet transform for C_N (b) highlighting the dominant $St = 0.17$ oscillation. Spanwise space-time plot (c) taken at $x/c_{\text{root}} = 0.5$ shows the alternating shedding behaviour.

0.6 with the co-existence of re-entrant jet and shockwave instabilities. This complex mix of shedding mechanisms has previously also been observed by de Graaf *et al.* (2017) and Smith *et al.* (2018). High-speed photography also reveals the presence of both mechanisms, where the shedding cycle starts with the typical re-entrant jet process with flow moving upstream under the cavity. However, due to the increased void fraction promoting shockwave propagation with the collapse of the previously shed cavity, the downstream extent of the cavity starts breaking up into a bubbly mixture as the shockwave propagates upstream. In the case of $0.5 \leqslant \sigma \leqslant 0.6$, the re-entrant jet is the primary driver of the shedding frequency with detachment of the cavity coming from shockwave propagation through the preconditioned flow. The SPOD intensity map for $\sigma = 0.4$ at $St = 0.11$ indicates that activity in the cavitation due to the shockwave is located at the downstream extent of the cavity, a region of relatively high-pressure. However, shockwave propagation is not evident in the space-time plots at a frequency of $St = 0.11$ with minimal amplitude in the wavelet transform component shown in figure 17b, despite appearing in the C_N PSD in figure 9. This is due to the intermittent nature of the global Type I shockwave instability being inactive for periods on the scale of seconds as can be seen in the wavelet transform from the medium type run at $\sigma = 0.4$ (figure 18). As the short type run acquisition is only one second in duration, the data presented in figure 17 has seemingly not included one of the intermittent Type I shockwave events. Alternatively, a space-time diagram produced from the medium run data, due to the reduced frame rate, lacks sufficient resolution to show clearly the Type I shockwave propagation.

Further reduction in σ to 0.3 sees the cavity grow to the point that the re-entrant jet driven Type IIa mode becomes no longer evident in the spectra (figure 9). High-speed photography reveals a re-entrant jet still forms, however, this has insufficient time and momentum to reach the upstream extent of the cavity before the shockwave, thus

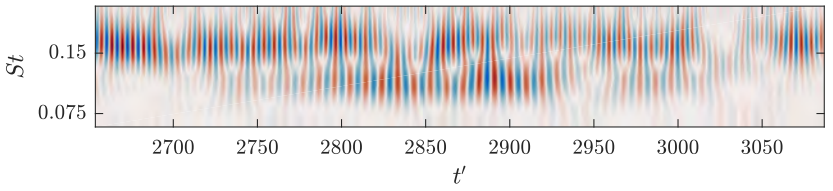

FIGURE 18. Real value of the Morlet wavelet transform for C_N from the medium duration run at $\sigma = 0.4$. The shockwave driven low mode ($St \approx 0.11$) is not continuously apparent through time, only being evident between $2800 \leqslant t' \leqslant 2950$.

preventing it from driving the shedding frequency. The shedding cycle is comprised of a complex set of events consisting of three main phases, a growth phase, a stable phase and a shockwave phase. These phases are noted as A, B and C, respectively, in the annotated chordwise space-time plot of figure 19e where the chordwise position is presented locally as x^*/c, where the streamwise position, x^*, is taken from the leading edge at the spanwise location and c is the local chord. The space-time plot shows that the growing cavity pauses once it reaches a point just downstream of the trailing-edge, remaining stable for a variable amount of time between cycles, ranging from $t' = 4.3$ to 10.7 in duration. This is followed by the attached cavity being broken up by upstream shockwave propagation. The propagation velocity is seen to change between cycles as indicated by the gradient of the red lines in figure 19e. The spanwise space-time plot (figure 19c) and supplementary movie 7 shows that a cycle also consists of a large-scale cloud that is shed from the upper portion of the span, shortly followed by approximately two small-scale clouds shed in quick succession from about mid-span. This shedding sequence also manifests in the SPOD phase map at $St = 0.09$ (figure 10) with small-scale clouds just below mid-span showing a significant phase difference in the high intensity region.

The frequency of the Type I mode does not vary significantly with σ. This is due to the shockwave initiation location being relatively invariant of σ and consequently the distance the shockwave must travel to break off the attached cavity. This is in contrast to the re-entrant jet which must travel the length of the attached cavity which does vary with σ. When acting exclusively, shockwave driven shedding is highly periodic as shown by the C_N wavelet transform in figure 19b exhibiting a consistent $St = 0.09$ excitation frequency through time, despite complex spanwise cavitation behaviour.

3.4.6. *Supercavitation*

The reduction of σ from 0.3 to 0.2 sees a significant growth in the cavity length to $L_c/c > 1.5$, now forming a supercavity (figure 5). Closing far downstream of the trailing-edge with no strong adverse pressure gradient present, the supercavity becomes more stable than partial cavities as no substantial shedding mechanisms can form. In addition, the associated turbulence and vortex shedding occur far enough downstream to have negligible influence on the hydrofoil and the forces it experiences (Brennen 1995).

The Type I mode disappears as the hydrofoil experiences supercavitation exhibiting no significant peaks in the C_N and $\delta/\bar{c}$ spectra (figure 9) as no large-scale shedding events are observed in the high-speed photography (supplementary movie 8), despite the vapour cavity remaining in a relatively high-pressure region. As mentioned previously, growth in the attached cavity leads to a higher void faction in the local flow, reducing the speed of sound below the local flow speed and allowing shockwave propagation. However, the speed of sound will actually increase in a liquid-vapour mixture if the void fraction is high enough (Shamsborhan *et al.* 2010). Reducing σ to 0.2 appears to have increased the void fraction sufficiently, inhibiting the remaining primary shedding instability from inducing

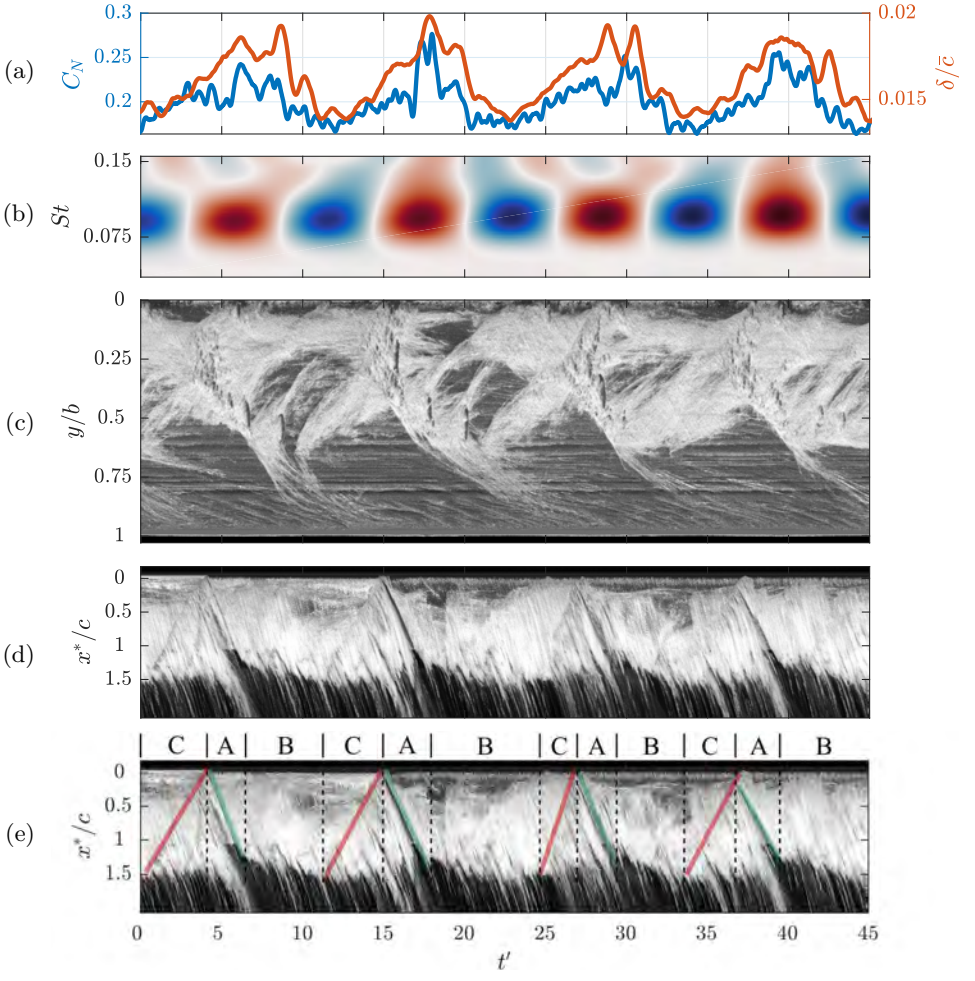

FIGURE 19. Synchronised time-series of the normal force (C_N) and tip displacement ($\delta/\bar{c}$) (a) at $\sigma = 0.3$, showing strong correlation, with the real value of the Morlet wavelet transform for C_N (b) highlighting the dominant $St = 0.09$ oscillation. Spanwise (c) and chordwise (d,e) space-time plots taken at $x/c_{\text{root}} = 0.5$ and $y/b = 0.25$, respectively, reveal that each cycle consists of a growth phase (A), indicated by green lines, a stable phase (B) and a shockwave phase (C), indicated by red lines in the annotated version of the chordwise space-time (e).

periodic cloud cavitation. With no instability to break up the attached cavity, the cavity grows significantly (figure 6), closing far downstream to form a stable supercavity.

3.4.7. *Spanwise cavity oscillation*

Experiments conducted on the same hydrofoils by Pearce *et al.* (2017) observed streamwise cavity oscillations not related to re-entrant jet or shockwave mechanisms, attributing them to spanwise tip excursions. The attached cavities are observed to oscillate, not just in the streamwise direction, but the spanwise direction as well, when the hydrofoil experiences cloud cavitation. Space-time plots taken around the quarter chord show the spanwise cavity oscillations which appear to be highly periodic (figure 20). They also do not appear to be directly related to shedding physics evident in the upper portion of the plots.

The spanwise growth and contraction of the cavity was recorded using a column of

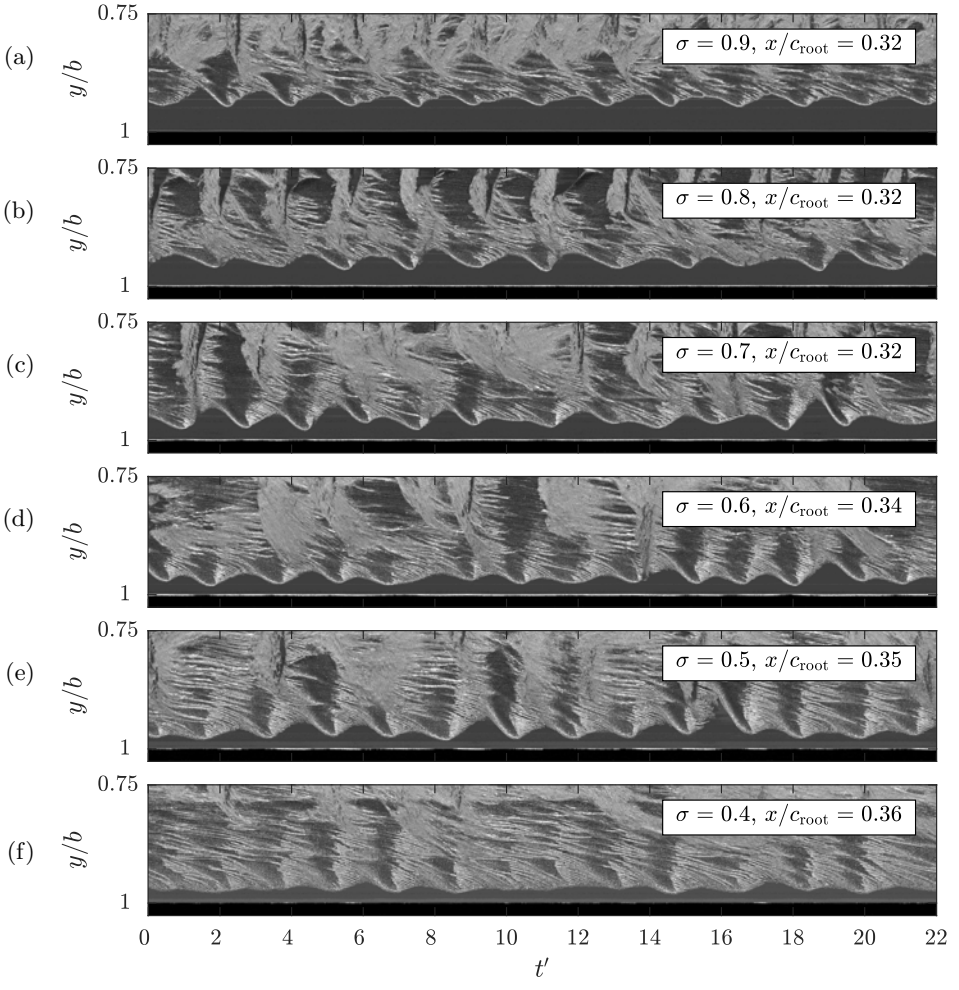

FIGURE 20. Spanwise space-time plots for various σ showing the spanwise cavity oscillation towards the tip of the hydrofoil. These oscillations are periodic and show a strong correlation with the tip displacement.

pixels at a specific chordwise location with tracking of the cavity extent achieved using the same edge detection method utilized for tip deflection measurements. Comparison of the PSD from the resulting time series with that of $\delta/\bar{c}$ (figure 21) reveals highly similar spectra, indicating a strong correlation between tip displacement and spanwise cavity oscillations. Additionally, apart from the lock-in phenomena (at $0.7 \leqslant \sigma \leqslant 0.75$), this is the only clear manifestation of structural excitations in the cavitation behaviour with the spanwise cavity oscillations being the only aspect exhibiting fluctuations for $St \geqslant 0.55$ that isn't attributed to shedding instabilities. This is an indication that the influence of FSI on the cavitation behaviour with the stainless steel model is almost inconsequential, and therefore reinforcing its validity to serve as a relatively stiff reference.

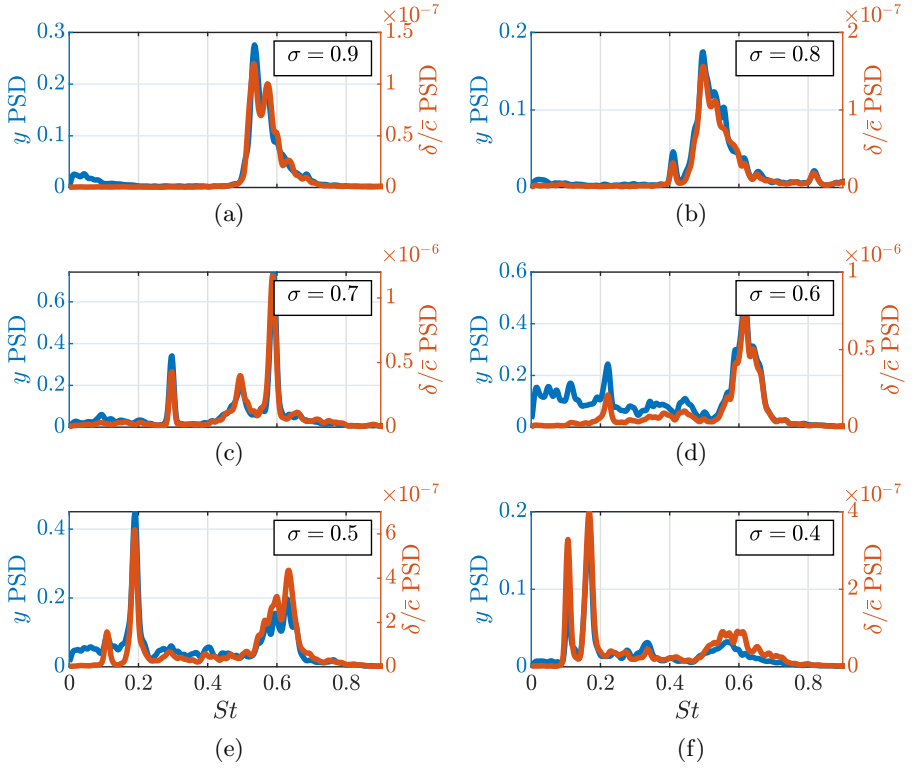

FIGURE 21. PSD of the spanwise cavity oscillations compared to that of the $\delta/\bar{c}$ showing similar spectral content at all σ, indicating a strong correlation between the two.

4. Conclusion

The behaviour of various cavitation regimes about a relatively stiff hydrofoil was investigated using high-speed photography and force measurements. Multiple cavitation regimes occurred in the cavitation number range tested, comprising of sheet, cloud and super-cavitation, each exhibiting unique traits. The instabilities driving the cavity shedding were identified from high-speed photography as either interfacial instabilities, re-entrant jet formation, shockwave propagation or as a complex, coupled mechanism, depending on the cavitation number. Three primary shedding modes were identified with the Type I shockwave driven shedding oscillating at a frequency nominally independent of σ. Re-entrant jet driven Type IIa & IIb oscillations exhibit a linear dependence on σ, decreasing in frequency with σ due to growth in cavity length. At higher cavitation numbers (> 1.0) where the cavity length is small, break-up is driven by small-scale interfacial instabilities that leads to small vapour pockets being shed. Reduction in σ to 1.0 moves the cavity closure into a region of sufficient adverse pressure gradient for a re-entrant jet to form and drive medium scale shedding from mid-span. For cavitation numbers between 0.9 and 0.7, the streamwise length of the cavity is geometrically compatible with the hydrofoil span to form two stable periodic shedding modes, Type IIa & IIb, driven by a re-entrant jet instability towards the root and tip, respectively. Decreasing the cavitation number below 0.6 sees the emergence of a shockwave instability with the cavity reaching the high-pressure region at the trailing-edge and reducing the local speed of sound below the local flow speed by increasing the void fraction. The re-entrant jet and shockwave instability occur concurrently, both causing complex shedding

physics and behaviour for $0.3 \leqslant \sigma \leqslant 0.6$ with the Type I shockwave driven shedding being the sole shedding mechanism remaining for $0.25 \leqslant \sigma \leqslant 0.3$. Further reduction in σ to 0.2 sees the cavity grow to a point that it closes far enough downstream to form a stable supercavity as no shedding mechanisms can form. Lock-in is seen to occur at $0.70 \leqslant \sigma \leqslant 0.75$ with the Type IIa shedding frequency matching the first sub-harmonic of the hydrofoil natural frequency in cavitating conditions. Despite lock-in, the structural deformations remained relatively small compared to hydrofoil dimensions and were observed to have minimal effect on the cavitating behaviour only manifesting in spanwise cavity oscillations. Hence, the stainless steel model provides a relatively stiff reference model for comparison with, and to aid in interpretation of, a more flexible hydrofoil of the same geometry. These results will be presented as a part 2 to the present report in a follow on publication.

Acknowledgements

This project was supported by the Research Training Centre of Naval Design and Manufacturing (RTCNDM), US Office of Naval Research (Dr. Ki-Han Kim, Program Officer) and ONR Global (Dr. Woei-Min Lin) through NICOP S&T Grant no. N62909-11-1-7013. The RTCNDM is a University-Industry partnership established under the Australian Research Council (ARC) Industry Transformation grant scheme (ARC IC140100003). The authors would like to acknowledge the assistance of Mr Steven Kent and Mr Robert Wrigley from the Australian Maritime College for their essential help with setting up and carrying out the experiments.

Declaration of Interests

The authors report no conflict of interest.

REFERENCES

Akcabay, D. T., Chae, E. J., Young, Y. L., Ducoin, A. & Astolfi, J. A. 2014 Cavity induced vibration of flexible hydrofoils. *Journal of Fluids and Structures* **49** (Supplement C), 463–484.

Akcabay, D. T. & Young, Y. L. 2014 Influence of cavitation on the hydroelastic stability of hydrofoils. *Journal of Fluids and Structures* **49**, 170–185.

Akcabay, D. T. & Young, Y. L. 2015 Parametric excitations and lock-in of flexible hydrofoils in two-phase flows. *Journal of Fluids and Structures* **57**, 344–356.

Arndt, Roger EA & Keller, AP 2003 A case study of international cooperation: 30 years of collaboration in cavitation research. In *ASME/JSME 2003 4th Joint Fluids Summer Engineering Conference*, pp. 153–166. American Society of Mechanical Engineers.

Ausoni, P., Farhat, M., Avellan, F., Escaler, X. & Egusquiza, E. 2005 Cavitation effects on fluid structure interaction in the case of a 2d hydrofoil. In *ASME 2005 Fluids Engineering Division Summer Meeting*, pp. 617–622. American Society of Mechanical Engineers.

Ausoni, P., Farhat, M., Escaler, X., Egusquiza, E. & Avellan, F. 2007 Cavitation influence on von karman vortex shedding and induced hydrofoil vibrations. *ASME J. Fluids Eng.* **129** (8), 966–973.

Avellan, F., Dupont, P. & Ryhming, I. L. 1988 Generation mechanism and dynamics of cavitation vortices downstream of a fixed leading edge cavity. In *17th Symposium on Naval Hydrodynamics*, pp. 1–13.

Bisplinghoff, R. L., Ashley, H. & Halfman, R. L. 1955 *Aeroelasticity*. Addison-Wesley Publishing Corporation.

Blevins, R. D. 1977 *Flow-induced vibration*. New York: Van Nostrand Reinhold Co.

Brandner, P. A. 2018 Microbubbles and cavitation: Microscales to macroscales. In *Keynote Lecture: Tenth International Symposium on Cavitation*, pp. 710–715.

Brandner, P. A., Lecoffre, Y. & Walker, G. J. 2007 Design considerations in the development of a modern cavitation tunnel. In *16th Australasian Fluid Mechanics Conference*, pp. 630–637.

Brandner, P. A., Walker, G. J., Niekamp, P. N. & Anderson, B. 2010 An experimental investigation of cloud cavitation about a sphere. *Journal of Fluid Mechanics* **656**, 147–176.

Brennen, C. E. 1969 The dynamic balances of dissolved air and heat in natural cavity flows. *Journal of Fluid Mechanics* **37** (1), 115–127.

Brennen, C. E. 1995 *Cavitation and Bubble Dynamics*. Oxford University Press.

Brennen, C. E. 2005 *Fundamentals of Multiphase Flow*. Cambridge University Press.

Brennen, C. E., Oey, K. T. & D., Babcock C. 1980 Leading-edge flutter of supercavitating hydrofoils. *Journal of Ship Research* **24** (3), 135–146.

Callenaere, M., Franc, J., Michel, J. & Riondet, M. 2001 The cavitation instability induced by the development of a re-entrant jet. *Journal of Fluid Mechanics* **444**, 223–256.

Ceccio, S. L. 2015 Mechanisms of sheet to cloud transition for partial cavities. In *Keynote Lecture in CAV 2015: 9th International Symposium on Cavitation*.

Clarke, D. B., Butler, D., Crowley, B. & Brandner, P. A. 2014 High-speed full-field deflection measurements on a hydrofoil using digital image correlation. In *30th Symposium on Naval Hydrodynamics*.

Crespo, A 1969 Sound and shock waves in liquids containing bubbles. *The Physics of Fluids* **12** (11), 2274–2282.

De La Torre, O., Escaler, X., Egusquiza, E. & Farhat, M. 2013 Experimental investigation of added mass effects on a hydrofoil under cavitation conditions. *Journal of Fluids and Structures* **39**, 173–187.

Ducoin, A., Astolfi, J. A. & Sigrist, J. 2012 An experimental analysis of fluid structure interaction on a flexible hydrofoil in various flow regimes including cavitating flow. *European Journal of Mechanics-B/Fluids* **36**, 63–74.

Foeth, E. J., Van Doorne, C. W. H., Van Terwisga, T. & Wieneke, B. 2006 Time resolved piv and flow visualization of 3d sheet cavitation. *Experiments in Fluids* **40** (4), 503–513.

Franc, J. 2001 Partial cavity instabilities and re-entrant jet. In *Keynote Lecture: Fourth International Symposium on Cavitation*.

Franc, J. & Michel, J. 2004 *Fundamentals of Cavitation*. Dordrecht: Kluwer Academic Publishers.

Furness, R. A. & Hutton, S. P. 1975 Experimental and theoretical studies of two-dimensional fixed-type cavities. *Journal of Fluids Engineering* p. 515.

Ganesh, H., Mäkiharju, S. A. & Ceccio, S. L. 2016 Bubbly shock propagation as a mechanism for sheet-to-cloud transition of partial cavities. *Journal of Fluid Mechanics* **802**, 37–78.

de Graaf, K. L., Brandner, P. A. & Pearce, B. W. 2017 Spectral content of cloud cavitation about a sphere. *Journal of Fluid Mechanics* **812**.

Harwood, C., Felli, M., Falchi, M., Garg, N., Ceccio, S. L. & Young, Y. L. 2019*a* The hydroelastic response of a surface-piercing hydrofoil in multiphase flows: Part I - Passive hydroelasticity. *Journal of Fluids and Structures - Submitted for review* .

Harwood, C., Felli, M., Falchi, M., Garg, N., Ceccio, S. L. & Young, Y. L. 2019*b* The hydroelastic response of a surface piercing hydrofoil in multiphase flows: Part II - Modal parameters and generalized fluid forces. *Journal of Fluids and Structures - Submitted for review* .

Ihara, A., Watanabe, H. & Shizukuishi, S. 1989 Experimental research of the effects of sweep on unsteady hydrofoil loadings in cavitation. *ASME J. Fluids Eng.* **111** (3), 263–270.

Jakobsen, J. K. 1964 On the mechanism of head breakdown in cavitating inducers. *Journal of Basic Engineering* **86** (2), 291–305.

Kaplan, P. & Lehman, A. F. 1966 Experimental studies of hydroelastic instabilities of cavitating hydrofoils. *Journal of Aircraft* **3** (3), 262–269.

Kato, Kazuhiko, Dan, Hirotaka & Matsudaira, Yasuaki 2006 Lock-in phenomenon of

pitching hydrofoil with cavitation breakdown. *JSME International Journal Series B Fluids and Thermal Engineering* **49** (3), 797–805.

Kawakami, D. T., Fuji, A., Tsujimoto, Y. & Arndt, R. E. 2008 An assessment of the influence of environmental factors on cavitation instabilities. *ASME J. Fluids Eng.* **130** (3), 031303.

Kawanami, Y., Kato, H. & Yamaguchi, H. 1998 Three-dimensional characteristics of the cavities formed on a two-dimensional hydrofoil. In *Third International Symposium on Cavitation*, , vol. 1, pp. 191–196. Laboratoire des Ecoulements Géophysiques et Industriels, Grenoble, France.

Kawanami, Y., Kato, H., Yamaguchi, H., Tanimura, M. & Tagaya, Y. 1997 Mechanism and control of cloud cavitation. *ASME J. Fluids Eng.* **119** (4), 788–794.

Kjeldsen, M. & Arndt, R. E. 2001 Joint time frequency analysis techniques: A study of transitional dynamics in sheet/cloud cavitation. In *4th International Symposium on Cavitation (CAV2001)*.

Kjeldsen, M., Arndt, R. E. A. & Effertz, M. 2000 Spectral characteristics of sheet/cloud cavitation. *ASME J. Fluids Eng.* **122** (3), 481–487.

Knapp, R. T. 1955 Recent investigations of the mechanics of cavitation and cavitation damage. *Transactions of the ASME* **77**, 1045–1054.

Kubota, A., Kato, H., Yamaguchi, H. & Maeda, M. 1989 Unsteady structure measurement of cloud cavitation on a foil section using conditional sampling technique. *ASME J. Fluids Eng.* **111** (2), 204–210.

Laberteaux, K. R. & Ceccio, S. L. 2001*a* Partial cavity flows. part 1. cavities forming on models without spanwise variation. *Journal of Fluid Mechanics* **431**, 1–41.

Laberteaux, K. R. & Ceccio, S. L. 2001*b* Partial cavity flows. part 2. cavities forming on test objects with spanwise variation. *Journal of Fluid Mechanics* **431**, 43–63.

de Lange, D. F. & de Bruin, G. J. 1998 Sheet cavitation and cloud cavitation, re-entrant jet and three-dimensionality. *Applied Scientific Research* **58** (1-4), 91–114.

Le, Q., Franc, J. & Michel, J. 1993 Partial cavities: Global behaviour and mean pressure distribution. *ASME J. Fluids Eng.* **115**, 243–243.

Leroux, J., Astolfi, J. A. & Billard, J. Y. 2004 An experimental study of unsteady partial cavitation. *ASME J. Fluids Eng.* **126** (1), 94–101.

Noordzij, L & Van Wijngaarden, L 1974 Relaxation effects, caused by relative motion, on shock waves in gas-bubble/liquid mixtures. *Journal of Fluid Mechanics* **66** (1), 115–143.

Pearce, B. W., Brandner, P. A., Garg, N., Young, Y. L., Phillips, A. W. & Clarke, D. B. 2017 The influence of bend-twist coupling on the dynamic response of cavitating composite hydrofoils. In *5th International Symposium on Marine Propulsors (SMP'17)*, pp. 803–813.

Pelz, P. F., Keil, T. & Gross, T. F. 2017 The transition from sheet to cloud cavitation. *Journal of Fluid Mechanics* **817**, 439–454.

Pham, T. M., Larrarte, F. & Fruman, D. H. 1999 Investigation of unsteady sheet cavitation and cloud cavitation mechanisms. *ASME J. Fluids Eng.* **121** (2), 289–296.

Prothin, S., Billard, J. & Djeridi, H. 2016 Image processing using proper orthogonal and dynamic mode decompositions for the study of cavitation developing on a naca0015 foil. *Experiments in Fluids* **57** (10), 157.

Reisman, G. E., Wang, Y. C. & Brennen, C. E. 1998 Observations of shock waves in cloud cavitation. *Journal of Fluid Mechanics* **355**, 255–283.

Russell, P. S., Venning, J. A., Brandner, P. A., Pearce, B. W., Giosio, D. R. & Ceccio, S. L. 2018 Microbubble disperse flow about a lifting surface. In *32nd Symposium on Naval Hydrodynamics*.

Schmidt, O. T., Towne, A., Rigas, G., Colonius, T. & Bres, G. A. 2018 Spectral analysis of jet turbulence. *Journal of Fluid Mechanics* **855**, 953–982.

Shamsborhan, H., Coutier-Delgosha, O., Caignaert, G. & Nour, F. A. 2010 Experimental determination of the speed of sound in cavitating flows. *Experiments in Fluids* **49** (6), 1359–1373.

Smith, S. M., Brandner, P. A., Pearce, B. W., Giosio, D. R. & Young, Y. L. 2019 Cloud cavitation behavior on a hydrofoil due to fluid-structure interaction. *ASME J. Fluids Eng.* **141** (4), 041105.

Smith, S. M., Venning, J. A., Brandner, P. A., Pearce, B. W., Giosio, D. R. & Young, Y. L. 2018 The influence of fluid-structure interaction on cloud cavitation about a hydrofoil. In *Proceedings of the 10th International Symposium on Cavitation (CAV2018)*. ASME Press.

Smith, S. M., Venning, J. A., Giosio, D. R., Brandner, P. A., Pearce, B. W. & Young, Y. L. 2017 Cloud cavitation behaviour on a hydrofoil due to fluid-structure interaction. In *17th International Symposium on Transport Phenomena and Dynamics of Rotating Machinery, ISROMAC 2017*.

Stutz, B. & Reboud, J. L. 1997 Experiments on unsteady cavitation. *Experiments in Fluids* **22** (3), 191–198.

Torrence, Christopher & Compo, Gilbert P 1998 A practical guide to wavelet analysis. *Bulletin of the American Meteorological Society* **79** (1), 61–78.

Towne, A., Schmidt, O. T. & Colonius, T. 2018 Spectral proper orthogonal decomposition and its relationship to dynamic mode decomposition and resolvent analysis. *Journal of Fluid Mechanics* **847**, 821–867.

Venning, James A, Giosio, Dean R, Pearce, Bryce W & Brandner, Paul A 2018*a* Global mode visualization in cavitating flows. In *Proceedings of the 10th International Symposium on Cavitation (CAV2018)*. ASME Press.

Venning, James A, Giosio, Dean R, Smith, Samuel M Pearce, Bryce W & Brandner, Paul A 2018*b* The influence of nucleation on the spectral content of cloud cavitation about a hydrofoil. In *Proceedings of the 10th International Symposium on Cavitation (CAV2018)*. ASME Press.

Venning, J. A., Khoo, M. T., Pearce, B. W. & Brandner, P. A. 2018*c* Background nuclei measurements and implications for cavitation inception in hydrodynamic test facilities. *Experiments in Fluids* **59** (4), 71.

Venning, James A, Smith, Samuel M, Brandner, Paul A, Giosio, Dean R & Pearce, Bryce W 2017 The influence of nuclei content on cloud cavitation about a hydrofoil. In *17th International Symposium on Transport Phenomena and Dynamics of Rotating Machinery, ISROMAC 2017*.

Welch, P. 1967 The use of fast fourier transform for the estimation of power spectra: a method based on time averaging over short, modified periodograms. *IEEE Transactions on Audio and Electroacoustics* **15** (2), 70–73.

Wu, J., Ganesh, H. & Ceccio, S. 2019 Multimodal partial cavity shedding on a two-dimensional hydrofoil and its relation to the presence of bubbly shocks. *Experiments in Fluids* **60** (4), 66.

Young, Y.L., Garg, N., Brandner, P.A., Pearce, B.W., Butler, D., Clarke, D. & Phillips, A.W. 2018 Material bend-twist coupling effects on cavitating response of composite hydrofoils. In *10th International Cavitation Symposium (CAV2018)*.

Zarruk, G. A., Brandner, P. A., Pearce, B. W. & Phillips, A. W. 2014 Experimental study of the steady fluid-structure interaction of flexible hydrofoils. *Journal of Fluids and Structures* **51**, 326–343.